

Hyperspectral Image Classification With Contrastive Graph Convolutional Network

Wentao Yu, *Student Member, IEEE*, Sheng Wan, Guangyu Li,
Jian Yang, *Member, IEEE* and Chen Gong, *Senior Member, IEEE*

Abstract—Recently, Graph Convolutional Network (GCN) has been widely used in Hyperspectral Image (HSI) classification due to its satisfactory performance. However, the number of labeled pixels is very limited in HSI, and thus the available supervision information is usually insufficient, which will inevitably degrade the representation ability of most existing GCN-based methods. To enhance the feature representation ability, in this paper, a GCN model with contrastive learning is proposed to explore the supervision signals contained in both spectral information and spatial relations, which is termed Contrastive Graph Convolutional Network (ConGCN), for HSI classification. First, in order to mine sufficient supervision signals from spectral information, a semi-supervised contrastive loss function is utilized to maximize the agreement between different views of the same node or the nodes from the same land cover category. Second, to extract the precious yet implicit spatial relations in HSI, a graph generative loss function is leveraged to explore supplementary supervision signals contained in the graph topology. In addition, an adaptive graph augmentation technique is designed to flexibly incorporate the spectral-spatial priors of HSI, which helps facilitate the subsequent contrastive representation learning. The extensive experimental results on six typical benchmark datasets firmly demonstrate the effectiveness of the proposed ConGCN in both qualitative and quantitative aspects.

Index Terms—Contrastive learning, Graph Convolutional Network (GCN), graph augmentation, Hyperspectral Image (HSI) classification.

I. INTRODUCTION

HYPERSPECTRAL Image (HSI) classification plays an increasingly significant role in environmental monitoring, precision agriculture, mineral identification, and land cover classification. Different from conventional remote sensing images, HSI is composed of diverse contiguous spectral bands, providing detailed spectral information in addition to spatial relations. This property is beneficial to attributing each pixel of HSI to a certain category.

In the past few decades, various methods have been proposed for HSI classification. The early-staged methods are

This research is supported by NSF of China (Nos: 61973162, 62006119), NSF of Jiangsu Province (No: BZ2021013), NSF for Distinguished Young Scholar of Jiangsu Province (No: BK20220080), the Fundamental Research Funds for the Central Universities (Nos: 30920032202, 30921013114), and CAAI-Huawei MindSpore Open Fund. (*Corresponding authors: Chen Gong; Guangyu Li.*)

The authors are with PCA Lab, Key Lab of Intelligent Perception and Systems for High-Dimensional Information of Ministry of Education, and Jiangsu Key Lab of Image and Video Understanding for Social Security, School of Computer Science and Engineering, Nanjing University of Science and Technology, Nanjing, 210094, P.R. China (e-mail: wentao.yu@njust.edu.cn; wan-sheng315@hotmail.com; liguangyu0627@hotmail.com; csjyang@njust.edu.cn; chen.gong@njust.edu.cn).

mainly based on conventional pattern recognition methods. In spite of the achievements obtained by these methods, they suffer from hand-crafted configurations. To avoid intricate feature engineering, deep learning-based methods can obtain high-level representations via gradually aggregating the low-level features, and have attracted increasing attention in recent years. As one of the most representative methods, Convolutional Neural Networks (CNN) have achieved state-of-the-art performance due to their powerful generalization ability. However, the receptive field of CNN is restricted by a regular square area, and thus CNN fail to adaptively capture the geometric variations of different land cover categories in HSI. To deal with this deficiency, recently, a number of Graph Convolutional Network (GCN) based HSI classification methods [1]–[5] have been proposed and achieved promising performance. For example, in [1], a multiscale dynamic GCN (MDGCN) was presented to obtain the dynamic graph and explore spectral-spatial correlations at multiple scales. Based on MDGCN, to tap into the advantage of contextual information, context-aware dynamic GCN [2] was proposed to further mine node features for HSI classification.

However, the representation ability of most existing GCN-based methods is still limited due to the following defects. First, the number of labeled pixels in HSI is usually insufficient in practical scenarios [6]–[9]. The supervision information provided by few labeled pixels is insufficient to train a GCN model with good discriminative ability [3]. Second, current GCN-based methods fail to exploit the long-range dependencies among image regions, as they mainly aim at encoding the pairwise importance among local image regions, which could lead to suboptimal performance [10].

To accommodate the above-mentioned issues, we propose a GCN-based method for HSI classification, termed “**Contrastive Graph Convolutional Network**” (ConGCN). First, we aim to sufficiently extract the supervision signals carried by the hyperspectral data themselves for network training. Concretely, we propose to use contrastive learning [11], [12] to encode the similarities among the spectral signatures of image regions. Contrastive learning is one of the representative self-supervised learning approaches and is able to generate data representations by learning to encode the similarities or dissimilarities among unlabeled examples. It has emerged as a powerful technique for graph representation learning recently [13], [14]. Different from the contrastive learning-based methods used in vision representation learning [11], [12], we design a semi-supervised contrastive loss to jointly extract supervision information from the scarce yet valuable

labeled data and the rich unlabeled data. To flexibly obtain different graph views for the contrastive learning model, we devise an adaptive graph augmentation technique by incorporating the spectral-spatial priors of HSI. In addition to the supervision signals contained in spectral features, the spatial relations among image regions are nonnegligible in HSI. Consequently, we develop a graph generative loss to model the relationship among spatially neighboring regions. This can be considered as a supplement to the supervision information extracted from spectral signatures. As such, the originally scarce supervision signals can be further enriched by exploring the knowledge from both spectral information and spatial relations of HSI, thereby leading to enhanced data representations. Besides, considering that conventional GCN models can only capture the localized dependencies among image regions [2], we propose to employ the localized and hierarchical graph convolution simultaneously. By doing so, both the local and global contextual information of HSI can be incorporated to help produce comprehensive representations.

In conclusion, the proposed ConGCN can exhaustively explore the supervision information contained in both spectral signatures and spatial relations of HSI by introducing the semi-supervised contrastive learning and graph generative loss. As a result, the abundant supervision information from hyperspectral data can facilitate the contrastive model training. Here, the spectral-spatial priors in HSI are exploited for adaptive data augmentation to produce meaningful contrastive pairs. Moreover, the contextual information at different spatial levels is jointly incorporated by employing localized and hierarchical graph convolution, which further helps enhance the representation power of the contrastive learning model.

To sum up, the contributions of our work are as follows:

- To the best of our knowledge, this is the first work to adopt a contrastive GCN model for HSI classification. Different from the existing GCN-based methods, which require sufficient label information for network training, our proposed ConGCN can exhaustively exploit the supervision information from hyperspectral data themselves to train the networks. Hence, the proposed method reveals a new type of GCN model that can perform well with very limited labeled pixels.
- The semi-supervised contrastive loss and graph generative loss are designed to exploit the supervision signals contained in the spectral domain and spatial relations of HSI, respectively.
- By performing localized and hierarchical graph convolution simultaneously, both local and global contextual information of HSI can be leveraged for expressive representation learning.
- We devise an adaptive graph augmentation technique by incorporating spectral-spatial priors, which helps boost the performance of contrastive learning.

The structure of this article is organized as follows. Section II reviews related typical prior works. Section III describes the pipeline of our proposed ConGCN method. Then the proposed method is presented in Section IV, Section V, and Section VI, which focuses on adaptive graph augmentation,

localized and hierarchical graph convolution, and the proposed loss functions, respectively. In addition, Section VII shows the experimental results of different methods on four widely-used datasets. Finally, Section VIII concludes this paper.

II. RELATED WORKS

This section reviews some typical prior works related to this paper, which include HSI classification methods, GCN models, and contrastive learning approaches.

A. HSI Classification Methods

During the past few decades, abundant methods have been put forward for HSI classification. The early-staged methods were mainly anchored on conventional machine learning methods, such as kernel-based methods [15], [16], recursive filtering [17], k -nearest-neighbor classifier [18], Support Vector Machine (SVM) [19], and Markov random field [20]. Unfortunately, they usually relied on empirically designed hand-crafted features, so their performances are often far from perfect.

To tackle this problem, a number of deep methods such as Generative Adversarial Networks (GAN) [21], [22] and CNN [23]–[26] have been further employed to promote HSI classification. For example, Feng *et al.* [21] introduced self-supervised learning to GAN for HSI classification by exploring abundant unlabeled examples, which helped improve the generation and classification abilities of the generator and discriminator, respectively. To reduce the dimensionality of HSI during classification, Feng *et al.* [26] developed an end-to-end CNN combining band selection, feature extraction, and classification for HSI. Despite the fact that the CNN-based methods display encouraging performances in some cases, they still have several defects. First of all, the receptive field of CNN is a regular square area, therefore CNN-based methods are unable to adaptively capture or perceive the geometric variations of different land cover categories in HSI. Besides, the weights of each convolution kernel are identical in different spectral bands. Consequently, the details of land cover boundaries are probably lost after feature abstraction, so the pixels around boundaries are likely to be misclassified due to the inflexible convolution kernel. As a sequel, more and more GCN-based HSI classification methods are proposed to address the above problems, which will be introduced below.

B. GCN and Its Application to HSI Classification

Graph Neural Network (GNN) [27] mapped the graph or its vertices to an Euclidean space via a transfer function. Owing to this, GNN is capable of processing graph-structured non-Euclidean data, therefore showing better flexibility and adaptability than CNN. After Bruna *et al.* [28] introduced graph Laplacian matrix for graph convolution, many GCN models have been proposed and obtained promising performance. Among these methods, Kipf and Welling [29] innovatively applied GCN to semi-supervised learning, which approximated spectral graph convolutions in a localized region so that the proposed method was able to learn hidden representation via encoding both graph structure and node features. However, it belongs to transductive methods, which fails to classify unseen

or newly-added nodes. To tackle with this issue, Hamilton *et al.* [30] developed an inductive framework termed GraphSAGE via generalizing the simple graph convolution to trainable aggregation functions.

For HSI classification, GCN is able to capture and preserve the boundaries of different land cover categories flexibly due to its good ability in processing non-Euclidean data. As a result, GCN-based HSI classification methods have emerged and attracted a lot of attention. To the best of our knowledge, Qin *et al.* [31] were the first to introduce GCN into HSI classification, which leveraged the features of both adjacency nodes in graph and the neighbor pixels in the HSI. To avoid the imprecise initial graph, Wan *et al.* [1] proposed to refine the graph gradually during the convolution process, so graph convolution was operated on a dynamic graph rather than a predefined fixed graph. To sufficiently explore the contextual information, Wan *et al.* [2] proposed the context-aware dynamic GCN to capture relations among the regions originally far away in the original spatial positions. To overcome the drawback of the manually constructed graph, Wan *et al.* developed a new dual interactive GCN to adaptively learn a discriminative region-induced graph [3]. In [4], a semi-supervised nonlocal graph convolutional network was developed to exploit labeled and unlabeled data, simultaneously. Moreover, Bai *et al.* [5] developed a deep attention GCN to mine HSI features via focusing on the spectral information which has a large impact on classification. Liu *et al.* [32] leveraged CNN to generate pixel-level features to enrich the superpixel-level features of GCN, and thus simultaneously taking the advantages of CNN and GCN. To fuse different-scale features from coarse to fine, Liu *et al.* [33] merged adjacent superpixels and then converted them into multilevel graphs. Then, a multilevel graph network was employed to exploit features of HSI from a hierarchical perspective.

However, the generalizability of most existing methods is usually limited due to their transductive setting. To solve this problem, Ding *et al.* [34] proposed a multiscale graph network combining GraphSAGE with context-aware learning to understand the global and local information in a graph. However, it only utilized spectral features to construct the graph. To incorporate the relationship between adjacent nodes at the stage of graph construction, Guo *et al.* [35] put forward a dual graph U-net via integrating spatial graph and spectral graph simultaneously.

Nonetheless, the representation ability of most existing GCN-based methods is still limited due to the inadequate labeled examples. To enhance the representation ability, in our work, we explore the supervision signals contained in spectral information by employing contrastive learning, as well as spatial relations by deploying GCN. Hence, the proposed method can obtain better classification results than existing methods.

C. Contrastive Learning

Contrastive learning is one of self-supervised representation learning methods, which aims to obtain discriminative feature representation by leveraging the similarities and dissimilarities

between examples [36]. It has gained increasing attention due to the promising results in various fields such as computer vision [11], [12] and natural language processing [37].

SimCLR [11] is a well-known contrastive learning method and is anchored on a Siamese network that learns latent representations via maximizing agreement between differently augmented views of the same example. Similar to SimCLR, MoCo [12] utilized InfoNCE loss [38] and stored negative examples by using a memory bank rather than a large mini-batch size.

The marriage of contrastive learning and GCN has also been observed in recent years. For example, Petar *et al.* [39] proposed to learn graph representations in an unsupervised manner via classifying local-global pairs and negative-sampled counterparts. Besides, to address the challenge of data heterogeneity in graphs, You *et al.* [40] developed graph contrastive learning with four types of graph data augmentations, each of which imposed certain prior on graph data and encoded the extent and pattern. Apart from this work, Peng *et al.* [41] introduced a novel concept of graphical mutual information for graph representation learning, which generalized the idea of conventional mutual information computations from vector space to the graph domain.

Nevertheless, these methods are not applicable to HSI classification studied in this paper, as they fail to consider the spatial and spectral cues which are naturally and uniquely inherited by HSIs. Besides, they also ignore the class information carried by a handful of labeled data for HSI classification. Consequently, in this paper, we devise a new contrastive GCN which is able to acquire discriminative representations for accurate HSI classification.

To the best of our knowledge, there have been two works [42], [43] employing contrastive learning for HSI classification. However, they simply use the traditional paradigm of contrastive learning by utilizing unlabeled examples for pre-training and fine-tuning the model with few labeled examples. In order to improve the discriminative power of the generated representations, our proposed method additionally incorporates the available class information by using a semi-supervised contrastive loss function. Furthermore, our proposed method incorporates spatial relations to the contrastive objective. As a result, the proposed ConGCN can produce more effective feature representations than ResNet-50 in [42] and the transformer model in [43]. The advantage of our ConGCN has also been empirically demonstrated in Section VII.

III. PIPELINE OF THE PROPOSED METHOD

This section describes the pipeline of our proposed ConGCN method (see Fig. 1). When an input HSI is given, it is firstly segmented into a set of compact image regions by using the Simple Linear Iterative Clustering (SLIC) algorithm [44]. Next, a graph (*i.e.*, \mathcal{G}) is constructed by treating each of the image regions as a graph node. After that, the proposed adaptive graph augmentation (Section IV) is conducted on this graph to obtain two augmented graphs (*i.e.*, $\tilde{\mathcal{G}}_1$ and $\tilde{\mathcal{G}}_2$). Finally, localized and hierarchical graph convolution (Section V) are performed based on the two augmented graphs to obtain node

TABLE I
SYMBOLS USED THROUGHOUT THIS PAPER.

Symbols	Description
\mathbf{X}	feature matrix of graph \mathcal{G}
$\mathbf{X}_{\text{labeled}}$	feature matrix of labeled examples
\mathbf{Y}	label matrix of graph \mathcal{G}
\mathbf{Z}	network output
\mathbf{x}_i	the i -th node in graph \mathcal{G}
d	feature dimension of \mathbf{x}_i
D	generalized Mahalanobis distance
I	mutual information

representations, where the semi-supervised contrastive loss (Section VI-A) and the graph generative loss (Section VI-B) are utilized for network training (Section VI-C).

As mentioned above, classical SLIC [44] algorithm is adopted to segment the entire HSI into a number of compact superpixels. This is because there are numerous image pixels in an HSI, and thus constructing a pixel-level graph could be extremely time-consuming. By using SLIC, each superpixel clustering a set of homogeneous pixels with strong spectral-spatial similarity is treated as a graph node. Here, the node features correspond to the average spectral signatures of the pixels involved in the corresponding superpixel. Hence, the number of graph nodes can be significantly reduced to improve the computational efficiency. Another benefit of using the superpixel segmentation is that the generated image regions can preserve the local structural information of HSI, as adjacent pixels with high spatial consistency usually have a large probability to belong to the same land cover category.

In our proposed GCN-based method, an undirected graph made up of $n = l + u$ nodes is defined as $\mathcal{G} = \langle \mathcal{V}, \mathcal{E} \rangle$, where $\mathcal{V} = \{\mathbf{x}_1, \dots, \mathbf{x}_l, \mathbf{x}_{l+1}, \dots, \mathbf{x}_n\}$ is the node set containing all examples (*i.e.*, superpixels), \mathcal{E} is the edge set modeling the connectivity among the nodes. In \mathcal{V} , the first l nodes are labeled, while the remaining u nodes are unlabeled. Note that the label of each superpixel is determined by the most frequent label within this superpixel. The adjacency matrix of \mathcal{G} denoted as \mathbf{A} can be calculated as

$$\mathbf{A}_{ij} = \begin{cases} e^{-\gamma \|\mathbf{x}_i - \mathbf{x}_j\|_2^2}, & \text{if } \mathbf{x}_i \in \mathcal{N}(\mathbf{x}_j) \text{ or } \mathbf{x}_j \in \mathcal{N}(\mathbf{x}_i) \\ 0, & \text{otherwise} \end{cases}, \quad (1)$$

where γ is a temperature parameter and is set to 0.2 according to [1]–[3], $\|\mathbf{x}_i - \mathbf{x}_j\|_2$ calculates the Euclidean distance between the graph nodes \mathbf{x}_i and \mathbf{x}_j , and $\mathcal{N}(\mathbf{x}_i)$ is the neighbor set of \mathbf{x}_i . Other important symbols used throughout this paper are listed in Table I.

IV. ADAPTIVE GRAPH AUGMENTATION

The core of contrastive learning is to maximize the agreement between differently augmented views of the same example, where data augmentation turns out to be an important prerequisite in contrastive learning. Nevertheless, how to obtain an augmentation technique that is beneficial to graph representation learning remains a challenge due to the non-Euclidean properties of graph-structured data. To address this issue, we propose an adaptive graph augmentation technique, which is able to incorporate spectral-spatial priors in HSI to

boost the performance of contrastive learning. Inspired by [45], the principle of our proposed graph augmentation method is to preserve important structures and attributes while perturbing possibly unimportant edges and features. The reason is that it will guide the model to ignore the noise introduced by unimportant edges and features, thus helping to learn important patterns underneath the input graph. To evaluate the importance of edges and features, we leverage generalized Mahalanobis distance [2] and mutual information [46], respectively, which will be later explained.

The proposed augmentation technique for each graph view is made up of the spatial-level graph augmentation (Section IV-A) and the spectral-level graph augmentation (Section IV-B). In the spatial-level graph augmentation, we adaptively emphasize the important edges while weakening unimportant edges, to preserve the intrinsic structure of the graph topology. In the spectral-level graph augmentation, we adaptively exchange the features of adjacent nodes, to explore diverse contexts across different graph views for contrastive learning and help the network obtain the improved representations.

A. Spatial-Level Graph Augmentation

In our proposed method, graph edges reflect the spatial relations among image regions and also constitute the topological structure of data. As a result, the edges are critical in ConGCN to yield good representations. However, most existing graph contrastive methods neglect the intrinsic topological properties of graphs when performing graph augmentation, since they uniformly drop the graph edges, which could result in sub-optimal performance. For example, removing some influential edges will deteriorate the graph topology and thus result in inaccurate representations. To tackle this problem, we aim to adaptively emphasize or weaken edges according to their influences in the graph.

First, we construct a generalized Mahalanobis distance D to measure the distance between each pair of nodes, which is formulated as

$$D(\mathbf{x}_i, \mathbf{x}_j) = \sqrt{(\mathbf{x}_i - \mathbf{x}_j)^\top \mathbf{W}_D \mathbf{W}_D^\top (\mathbf{x}_i - \mathbf{x}_j)}, \quad (2)$$

where \mathbf{W}_D denotes a trainable weight matrix. This distance could be utilized to estimate the edge influence between each pair of nodes. Specifically, a small distance $D(\mathbf{x}_i, \mathbf{x}_j)$ often corresponds to a minor edge influence of the edge between \mathbf{x}_i and \mathbf{x}_j . Anchored on Eq. (2), to adaptively emphasize or weaken the edges, we modify the original adjacency matrix \mathbf{A} by adding an auxiliary matrix \mathbf{A}' , which can be calculated as

$$\mathbf{A}'_{ij} = \begin{cases} -\min(e^{D(\mathbf{x}_i, \mathbf{x}_j)-\tau}, e^\tau) + 1, & \text{if } D(\mathbf{x}_i, \mathbf{x}_j) > \tau \\ e^{-D(\mathbf{x}_i, \mathbf{x}_j)+\tau} - 1, & \text{if } D(\mathbf{x}_i, \mathbf{x}_j) \leq \tau \end{cases}, \quad (3)$$

where $\mathbf{x}_i \in \mathcal{N}(\mathbf{x}_j)$ or $\mathbf{x}_j \in \mathcal{N}(\mathbf{x}_i)$, $\tau > 0$ is a learnable parameter, and the truncation parameter e^τ is used to avoid excessively large values. Visual explanation of Eq. (3) is shown in Fig. 2, where τ is a threshold. As can be observed in Fig. 2, when $D(\mathbf{x}_i, \mathbf{x}_j) \leq \tau$, the edge between \mathbf{x}_i and \mathbf{x}_j may have a large influence on the graph and thus could be emphasized.

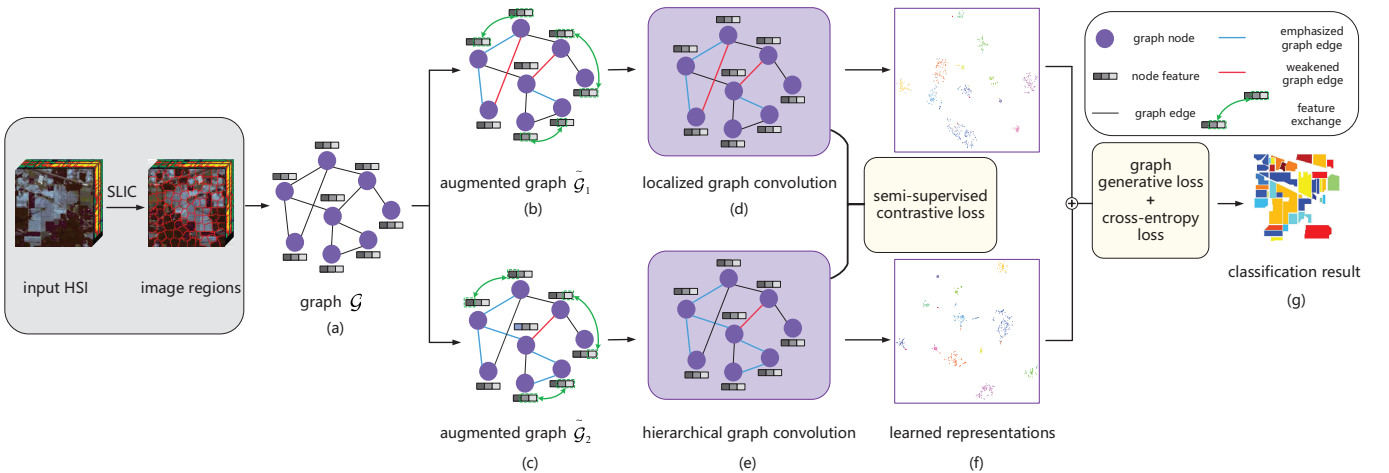


Fig. 1. Framework of our proposed ConGCN. In this figure, purple circles and black lines represent graph nodes and edges, respectively. In (a), a graph \mathcal{G} is constructed over the image regions produced by SLIC algorithm. The notations $\tilde{\mathcal{G}}_1$ and $\tilde{\mathcal{G}}_2$ in (b) and (c) denote two different graph views generated by the proposed adaptive graph augmentation technique. In (b) and (c), the blue lines and red lines represent emphasized edges and weakened edges, respectively. Besides, the green arrows denote the exchange of node features. (d) and (e) represent localized graph convolution and hierarchical graph convolution, respectively. The semi-supervised contrastive loss is computed across the two graph views. (f) denotes the node representations learned from the two views. In (g), the classification result is acquired via integrating the learned representations. Here, cross-entropy loss is used to penalize the difference between the output and the labels of the initially labeled seed superpixels. In the meanwhile, the graph generative loss is employed to exploit the topological information of the graph.

In contrast, when $D(\mathbf{x}_i, \mathbf{x}_j) > \tau$, the corresponding edge could be weakened, considering its minor influence on the graph. In addition, the function curve is truncated to $-e^\tau + 1$ when $D(\mathbf{x}_i, \mathbf{x}_j) > 2\tau$, to avoid excessively small values. To construct a randomly augmented graph view, we then generate a random masking matrix $\tilde{\mathbf{R}} \in \{0, 1\}^{n \times n}$. Here, the element $\tilde{\mathbf{R}}_{ij} = \tilde{\mathbf{R}}_{ji}$ is sampled from a Bernoulli distribution $B(1, p_{\text{sample}})$ if $i \neq j$, and the value of each diagonal element $\tilde{\mathbf{R}}_{ii}$ is fixed to one. The hyperparameter p_{sample} denotes the probability of performing edge emphasizing or weakening. Afterwards, the adjacency matrix $\tilde{\mathbf{A}}$ of the augmented graph can be computed as

$$\tilde{\mathbf{A}} = \mathbf{A} + \mathbf{A}' \circ \tilde{\mathbf{R}}, \quad (4)$$

where \circ denotes Hadamard product. By using Eq. (4), the spatial-level graph augmentation can be performed on the randomly sampled edges. Next, for \mathbf{x}_i and \mathbf{x}_j satisfying $\mathbf{x}_i \in \mathcal{N}(\mathbf{x}_j)$ or $\mathbf{x}_j \in \mathcal{N}(\mathbf{x}_i)$, the corresponding element $\tilde{\mathbf{A}}_{ij}$ can be normalized to $[0, 1]$ by

$$\tilde{\mathbf{A}}_{ij} \leftarrow \frac{\tilde{\mathbf{A}}_{ij} - \tilde{\mathbf{A}}_{\min}}{\tilde{\mathbf{A}}_{\max} - \tilde{\mathbf{A}}_{\min}}, \quad (5)$$

where $\tilde{\mathbf{A}}_{\min}$ and $\tilde{\mathbf{A}}_{\max}$ are the minimum and the maximum values of $\tilde{\mathbf{A}}_{ij}$, respectively. With Eq. (5), we can make all the values of $\tilde{\mathbf{A}}$ no less than 0. Therefore, by employing the spatial-level augmentation, the graph edges can be adaptively emphasized or weakened according to their corresponding importance.

B. Spectral-Level Graph Augmentation

Different from the spatial-level graph augmentation that focuses on the spatial relations of image regions in HSI, our proposed spectral-level augmentation aims to perturb the spectral signatures (*i.e.*, node features) for graph augmentation.

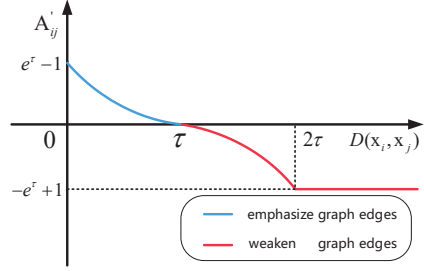


Fig. 2. Visual explanation of Eq. (3). The horizontal axis corresponds to $D(\mathbf{x}_i, \mathbf{x}_j)$ and the vertical axis corresponds to A'_{ij} . When $A'_{ij} > 0$ (drawn in blue), the original graph edges will be emphasized as the value of A'_{ij} is positive; when $A'_{ij} < 0$ (drawn in red), the original graph edges will be weakened as the value of A'_{ij} is negative.

To achieve this target, [39] uniformly shuffles node features for graph augmentation, which actually treats all feature dimensions equally and ignores their distinct contributions. Inspired by chromosomal crossover [47]–[49] in biology, we come up with a new augmentation method that exchanges partial dimensions of node features according to the spectral information of HSI.

Chromosomal crossover represents the exchange of genetic material at the stage of sexual reproduction between two homologous chromosomes' non-sister chromatids, which leads to recombinant chromosomes and significantly increases genetic diversity [50]. Schematic diagram of chromosomal crossover is shown in Fig. 3(a). For spectral-level graph augmentation, we treat two adjacent nodes as homologous chromosomes' non-sister chromatids and regard their node features as genetic material. Then partial exchange of node features is performed across the graph edges, which is shown in Fig. 3(b). The aim of feature exchange is to provide diverse perturbations for contrastive learning and guide the network to obtain improved

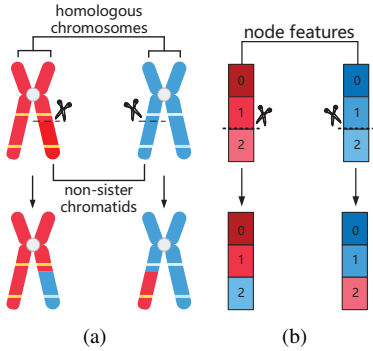


Fig. 3. The analogy of chromosomal crossover and feature exchange. (a) is the illustration of the exchange of genetic material during sexual reproduction between two homologous chromosomes' non-sister chromatids. (b) is the illustration of spectral-level graph augmentation. In (b), the colored small rectangles represent node features, where "0", "1", and "2" in the figure represent the IDs of different dimensions. Here, the features are exchanged at the dimension with ID "2".

representation. Notably, the feature exchange is limited in the adjacent nodes (*i.e.*, the nodes connected by the edges of \mathcal{G}) to avoid corrupting the essential structure of graphs.

Motivated by [45], features in influential dimensions are expected to be exchanged with small probability, as they often carry valuable spectral information that is beneficial to accurate classification. In the proposed spectral augmentation, we firstly generate a random vector \mathbf{m} with the h -th element \mathbf{m}_h ($h = 1, 2, \dots, d$) drawn from a Bernoulli distribution independently, namely $\mathbf{m}_h \sim B(1, 1 - p_h)$, where the parameter p_h reflects the importance of the h -th feature dimension. Afterwards, feature exchange between each pair of nodes will be performed at the h -th dimension if $\mathbf{m}_h = 1$. Here, the parameter p_h is obtained by mutual information, since the mutual information $I(\mathbf{X}_{\text{labeled}[:,h]}, \mathbf{Y})$ is able to characterize the relationship between the h -th feature dimension of $\mathbf{X}_{\text{labeled}}$ (*i.e.*, $\mathbf{X}_{\text{labeled}[:,h]}$) and the label matrix \mathbf{Y} . The notation $\mathbf{X}_{\text{labeled}}$ denotes the features of l labeled examples. The notation $\mathbf{Y} \in \mathbb{R}^{l \times c}$ represents the label matrix, where c is the number of land cover categories. The element $\mathbf{Y}_{ij} = 1$ if the i -th labeled example belongs to the j -th land cover category, and $\mathbf{Y}_{ij} = 0$, otherwise. However, it could be difficult to directly calculate $I(\mathbf{X}_{\text{labeled}[:,h]}, \mathbf{Y})$, as the probability distribution of $\mathbf{X}_{\text{labeled}[:,h]}$ is unavailable. Fortunately, according to [46], $I(\mathbf{X}_{\text{labeled}[:,h]}, \mathbf{Y})$ can be estimated by partitioning them into bins of finite size and approximated via the finite sum. As a result, we partition $\mathbf{X}_{\text{labeled}[:,h]}$ and \mathbf{Y} into N bins, where $n_x(i)$ and $n_y(j)$ represent the number of examples falling into the i -th bin of $\mathbf{X}_{\text{labeled}[:,h]}$ and the j -th bin of \mathbf{Y} , respectively. The notation $n(i, j)$ denotes the number of examples in their intersection. Consequently, $I(\mathbf{X}_{\text{labeled}[:,h]}, \mathbf{Y})$ can be estimated as

$$I(\mathbf{X}_{\text{labeled}[:,h]}, \mathbf{Y}) \approx \sum_{i,j} p(i, j) \log \frac{p(i, j)}{p_x(i)p_y(j)}, \quad (6)$$

where $p_x(i) \approx \frac{n_x(i)}{N}$, $p_y(j) \approx \frac{n_y(j)}{N}$, and $p(i, j) \approx \frac{n(i, j)}{N}$. According to the definition of mutual information, the h -th feature dimension is important in determining the land cover category if the value of $I(\mathbf{X}_{\text{labeled}[:,h]}, \mathbf{Y})$ is large. As a result, we can let $p_h = I(\mathbf{X}_{\text{labeled}[:,h]}, \mathbf{Y})$ ($h = 1, 2, \dots, d$) after

normalizing $I(\mathbf{X}_{\text{labeled}[:,h]}, \mathbf{Y})$ to $[0, 1]$.

It is notable that for each graph node, the spectral-level augmentation can be performed no more than once to avoid excessive damage to graph information. Meanwhile, the spectral-level augmentation will be performed on the node pairs in descending order by the value of A_{ij} , with the expectation that feature exchange across similar nodes can probably preserve the original topological information.

V. LOCALIZED AND HIERARCHICAL GRAPH CONVOLUTION

In HSI, the image regions that are far away in the original 2D space may belong to the same land cover category. However, most existing GCN models fail to exploit the long-range dependencies among image regions, as they mainly aim at encoding the pairwise importance among local image regions, which could lead to degraded performance. To deal with this issue, we propose to use localized and hierarchical graph convolution, simultaneously, so as to incorporate both local and global contextual information.

A. Localized Graph Convolution

There are various outstanding GCN architectures available to obtain representations from the local view, such as the well-known GCN [29] and graph attention network [51]. For simplicity, we select the classical GCN to perform localized graph convolution. The convolution process can be denoted as

$$\mathbf{Z}^{\text{local}} = \hat{\mathbf{A}}\sigma\left(\hat{\mathbf{A}}\mathbf{X}_1\mathbf{W}^{(0)}\right)\mathbf{W}^{(1)}, \quad (7)$$

where $\hat{\mathbf{A}} = \tilde{\mathbf{D}}^{-\frac{1}{2}}\bar{\mathbf{A}}\tilde{\mathbf{D}}^{-\frac{1}{2}}$ is leveraged to normalize the adjacency matrix, $\bar{\mathbf{A}} = \mathbf{A}_1 + \mathbf{I}$ is used to add the self-connection to adjacency matrix, \mathbf{A}_1 is the adjacency matrix of $\tilde{\mathcal{G}}_1$, \mathbf{I} is the identity matrix, and $\tilde{\mathbf{D}}_{ii} = \sum_j \bar{\mathbf{A}}_{ij}$. In Eq. (7), $\mathbf{W}^{(0)}$ and $\mathbf{W}^{(1)}$ indicate the learnable weight matrices, $\sigma(\cdot)$ denotes the activation function (*i.e.*, ReLU [52] in our ConGCN), $\mathbf{X}_1 \in \mathbb{R}^{n \times d}$ represents the feature matrix of $\tilde{\mathcal{G}}_1$, and $\mathbf{Z}^{\text{local}}$ represents the representations learned from the local view.

B. Hierarchical Graph Convolution

To incorporate the global contextual information of HSI, we adopt the Hierarchical Graph Convolutional Network (HGCN) [53] to perform hierarchical graph convolution. Generally speaking, HGCN aggregates the nodes with similar structures to a set of hyper-nodes constantly. Therefore, it is able to generate coarsened graphs via successive convolution and enlarge the receptive field. In addition, the symmetric graph refining layers are utilized to reconstruct the original graph topology for node-level representation. By this means, the global contextual information can be gradually encoded via hierarchical graph convolution. Hence, the representations $\mathbf{Z}^{\text{global}}$ generated from the global view can well complement to $\mathbf{Z}^{\text{local}}$ and help improve the representation ability of the proposed method.

VI. LOSS FUNCTION

In this section, we introduce the loss functions employed by our method.

A. Semi-Supervised Contrastive Loss Function

In the proposed ConGCN, we intend to leverage the abundant spectral information to help guide the model training. Fortunately, contrastive learning can naturally exploit the spectral signatures of HSI to generate representations. However, the traditional unsupervised contrastive loss [54] can only utilize unlabeled data for model training, which might ignore the precious label information of HSI. To cope with this issue, we devise a semi-supervised contrastive loss to improve the discriminative power of generated representation. Specifically, it can be divided into two parts, *i.e.*, the unsupervised and supervised contrastive losses, respectively.

Here, the unsupervised loss in the local graph view $\mathcal{L}_{\text{uc}}^{\text{local}}(\mathbf{x}_i)$ can be calculated as Eq. (8). Analogously, the unsupervised loss in the global graph view $\mathcal{L}_{\text{uc}}^{\text{global}}(\mathbf{x}_i)$ can be calculated by Eq. (9) as follows:

$$\mathcal{L}_{\text{uc}}^{\text{local}}(\mathbf{x}_i) = -\frac{1}{2n} \log \frac{e^{\langle \mathbf{z}_i^{\text{local}}, \mathbf{z}_i^{\text{global}} \rangle}}{\sum_{j=1}^n e^{\langle \mathbf{z}_i^{\text{local}}, \mathbf{z}_j^{\text{global}} \rangle}}, \quad (8)$$

$$\mathcal{L}_{\text{uc}}^{\text{global}}(\mathbf{x}_i) = -\frac{1}{2n} \log \frac{e^{\langle \mathbf{z}_i^{\text{global}}, \mathbf{z}_i^{\text{local}} \rangle}}{\sum_{j=1}^n e^{\langle \mathbf{z}_i^{\text{global}}, \mathbf{z}_j^{\text{local}} \rangle}}, \quad (9)$$

where $\mathbf{z}_i^{\text{local}} = \mathbf{Z}_{i,:}^{\text{local}}$ and $\mathbf{z}_i^{\text{global}} = \mathbf{Z}_{i,:}^{\text{global}}$ indicate the representations of \mathbf{x}_i learned from local and global views, respectively, and $\langle \cdot \rangle$ expresses the inner product. The notation $\mathbf{Z}_{i,:}^{\text{local}}$ and $\mathbf{Z}_{i,:}^{\text{global}}$ denote the i -th row of $\mathbf{Z}^{\text{local}}$ and $\mathbf{Z}^{\text{global}}$, respectively.

To exploit the scarce yet valuable class information for model training, the supervised contrastive loss function can be defined as

$$\mathcal{L}_{\text{sc}}^{\text{local}}(\mathbf{x}_i) = -\frac{1}{2l} \log \frac{\sum_{k=1}^l \mathbb{1}_{[y_i=y_k]} e^{\langle \mathbf{z}_i^{\text{local}}, \mathbf{z}_k^{\text{global}} \rangle}}{\sum_{j=1}^l e^{\langle \mathbf{z}_i^{\text{local}}, \mathbf{z}_j^{\text{global}} \rangle}}, \quad (10)$$

$$\mathcal{L}_{\text{sc}}^{\text{global}}(\mathbf{x}_i) = -\frac{1}{2l} \log \frac{\sum_{k=1}^l \mathbb{1}_{[y_i=y_k]} e^{\langle \mathbf{z}_i^{\text{global}}, \mathbf{z}_k^{\text{local}} \rangle}}{\sum_{j=1}^l e^{\langle \mathbf{z}_i^{\text{global}}, \mathbf{z}_j^{\text{local}} \rangle}}, \quad (11)$$

where $\mathcal{L}_{\text{sc}}^{\text{local}}(\mathbf{x}_i)$ and $\mathcal{L}_{\text{sc}}^{\text{global}}(\mathbf{x}_i)$ represent the supervised pairwise contrastive losses of \mathbf{x}_i in local and global views, respectively, $\mathbb{1}_{[\cdot]}$ is an indicator function which equals to 1 if the argument inside the bracket holds and 0, otherwise. In Eq. (10) and Eq. (11), y_i and y_k are the labels of \mathbf{x}_i and \mathbf{x}_k , respectively. Different from the unsupervised contrastive loss in Eq. (8) and Eq. (9), the positive and negative pairs in Eq. (10) and Eq. (11) can also be constructed based on the class information. That is to say, the nodes belonging to identical/different class are regarded as positive/negative pair.

In consequence, the proposed semi-supervised contrastive loss function \mathcal{L}_{ssc} can be represented as

$$\mathcal{L}_{\text{ssc}} = \sum_{i=1}^n (\mathcal{L}_{\text{uc}}^{\text{local}}(\mathbf{x}_i) + \mathcal{L}_{\text{uc}}^{\text{global}}(\mathbf{x}_i)) + \sum_{i=1}^l (\mathcal{L}_{\text{sc}}^{\text{local}}(\mathbf{x}_i) + \mathcal{L}_{\text{sc}}^{\text{global}}(\mathbf{x}_i)). \quad (12)$$

By minimizing \mathcal{L}_{ssc} , our proposed ConGCN can enhance the discriminative power of generated representations and further improve the subsequent HSI classification result.

B. Graph Generative Loss Function

In addition to the spectral information exploited by contrastive learning, we also intend to implicitly leverage spatial relations to better guide the representation learning process. Here, the graph generative loss function is designed to explore supervision signals from the spatial relations among image regions, which can lead to enhanced data representations and improved classification results.

Motivated by the generative models [55], we create a binary random variable e_{ij} which equals to 1 if there is an edge between \mathbf{x}_i and \mathbf{x}_j , and 0, otherwise. We presume that e_{ij} is conditionally independent, so given $\mathbf{Z}^{\text{local}}$ and $\mathbf{Z}^{\text{global}}$, the conditional probability of the input graph \mathcal{G} can be expressed by maximizing the following likelihood estimation:

$$p(\mathcal{G} | \mathbf{Z}^{\text{local}}, \mathbf{Z}^{\text{global}}) = \prod_{i,j} p(e_{ij} | \mathbf{Z}^{\text{local}}, \mathbf{Z}^{\text{global}}). \quad (13)$$

Furthermore, we reasonably assume that the probability of e_{ij} only depends on the representations of \mathbf{x}_i and \mathbf{x}_j according to [55]. As a result, the conditional probability of e_{ij} can be computed as $p(e_{ij} | \mathbf{Z}^{\text{local}}, \mathbf{Z}^{\text{global}}) = p(e_{ij} | \mathbf{z}_i^{\text{local}}, \mathbf{z}_j^{\text{global}})$.

In the end, the logistic function is utilized to encode the above-mentioned conditional probability, which turns out to be

$$\begin{aligned} p(\mathcal{G} | \mathbf{Z}^{\text{local}}, \mathbf{Z}^{\text{global}}) &= \prod_{i,j} p(e_{ij} | \mathbf{z}_i^{\text{local}}, \mathbf{z}_j^{\text{global}}) \\ &= \prod_{i,j} \delta([\mathbf{z}_i^{\text{local}}, \mathbf{z}_j^{\text{global}}] \mathbf{w}), \end{aligned} \quad (14)$$

where $\delta(\cdot)$ denotes the logistic function, \mathbf{w} represents a trainable parameter vector, and $[\cdot, \cdot]$ denotes the concatenation operation. Consequently, the proposed graph generative loss function can be represented as $\mathcal{L}_{g^2} = -p(\mathcal{G} | \mathbf{Z}^{\text{local}}, \mathbf{Z}^{\text{global}})$, which is used by our proposed ConGCN to extract precious yet implicit spatial relations among image regions in HSI.

C. Model Training

After integrating the graph representation from global and local graph views, the final output of our proposed ConGCN can be computed as $\mathbf{O} = \lambda_{\text{local}} \mathbf{Z}^{\text{local}} + (1 - \lambda_{\text{local}}) \mathbf{Z}^{\text{global}}$, where $0 < \lambda_{\text{local}} < 1$ denotes the weight assigned to $\mathbf{Z}^{\text{local}}$. In addition, the cross-entropy loss function $\mathcal{L}_{\text{ce}} = -\sum_{i=1}^l \sum_{j=1}^c \mathbf{Y}_{ij} \ln \mathbf{O}_{ij}$ is utilized to penalize the label differences between the final output \mathbf{O} and the initially labeled seed superpixels.

Finally, the overall loss function of our proposed ConGCN is shown in Eq. (15) via assembling the cross-entropy loss function \mathcal{L}_{ce} , semi-supervised contrastive loss function \mathcal{L}_{ssc} , and graph generative loss function \mathcal{L}_{g^2} , namely

$$\mathcal{L} = \mathcal{L}_{\text{ce}} + \lambda_{\text{ssc}} \mathcal{L}_{\text{ssc}} + \lambda_{g^2} \mathcal{L}_{g^2}, \quad (15)$$

where $\lambda_{\text{ssc}} > 0$ and $\lambda_{g^2} > 0$ are hyperparameters adjusting the impact of \mathcal{L}_{ssc} and \mathcal{L}_{g^2} , respectively. The process of the proposed ConGCN is exhibited in Algorithm 1.

VII. EXPERIMENTS

To demonstrate the effectiveness of our proposed ConGCN, intensive experiments are conducted on four well-known HSI datasets, namely *Indian Pines*, *University of Pavia*, *Salinas*,

Algorithm 1 The proposed ConGCN algorithm.

Input: Feature matrix \mathbf{X} ; label matrix \mathbf{Y} ; maximum number of iterations \mathcal{T} .
Output: Predicted label for each unlabeled graph node.

- 1: **for** $t = 1$ to \mathcal{T} **do**
- 2: Generate two augmented graphs $\tilde{\mathcal{G}}_1$ and $\tilde{\mathcal{G}}_2$;
- 3: Perform localized and hierarchical graph convolution to obtain graph representation $\mathbf{Z}^{\text{local}}$ and $\mathbf{Z}^{\text{global}}$, respectively;
- 4: Compute semi-supervised contrastive loss function \mathcal{L}_{ssc} via Eq. (12);
- 5: Compute graph generative loss function \mathcal{L}_{g^2} ;
- 6: Compute cross-entropy loss \mathcal{L}_{ce} ;
- 7: Update network parameters via operating back propagation according to overall loss function \mathcal{L} in Eq. (15);
- 8: $t := t + 1$;
- 9: **end for**
- 10: Predict labels based on the trained network.

and *Houston University* datasets, of which the details are introduced in the appendix. Concretely, we first compare our proposed ConGCN with other state-of-the-art methods using four metrics according to [1]–[3], namely per-class accuracy, overall accuracy (OA), average accuracy (AA), and kappa coefficient. After that, ablative experiments are carried out to evaluate the effectiveness of semi-supervised contrastive loss function, graph generative loss function, and our proposed graph augmentation technique. To further evaluate the effectiveness of our proposed method, we conduct experiments on two additional datasets: *WHU-Hi-HanChuan* and *WHU-Hi-HongHu* datasets [56], [57], which are presented in the appendix. Meanwhile, to reveal the advantage of our proposed ConGCN over the baseline methods in terms of efficiency, we report the training and inferring time of the proposed ConGCN and the compared baseline methods, which are presented in the appendix.

A. Experimental Settings

In our experiments, the proposed ConGCN is implemented by TensorFlow with Adam optimizer. For each dataset, 30 labeled pixels (*i.e.*, examples) of HSI are randomly selected in each land cover category for training. If there are less than 30 examples, only 15 labeled examples are chosen for the corresponding land cover category. In the training phase, 90% of the labeled examples are utilized to train the network parameters and 10% of the labeled examples are leveraged as validation set to fine-tune the hyperparameters (*e.g.*, λ_{local} and λ_{ssc}). All unlabeled examples are used for testing to evaluate the classification performance. The network architecture of our proposed ConGCN is kept identical for all datasets. Moreover, the learning rate and the maximum number of iterations are set to 0.01 and 4000, respectively.

To demonstrate the effectiveness of our proposed ConGCN method, other state-of-the-art HSI classification methods are also utilized for comparison. Concretely, we adopt three GCN-based methods, namely, dual-level deep Spatial Manifold Representation (SMR) network [58], Multilevel Super-

pixel Structured Graph U-net (MSSGU) [33], and Superpixel Graph Learning (SGL) [59]. Besides, one contrastive learning based method [42] termed “Self-Supervised Contrastive Learning” (SSCL) is employed for comparison. In addition, we incorporate two CNN-based methods, namely, Attention-based Adaptive Spectral-Spatial Kernel (A²S²K) [24] and Adaptive Spectral-Spatial Multiscale Network (ASSMN) [25]. The compared baseline methods also include one generative based method, *i.e.*, Adaptive Dropblock-enhanced Generative Adversarial Network (ADGAN) [22]. Besides, the proposed ConGCN is compared with four traditional HSI classification methods, namely, Multiple Feature Learning (MFL) [60], Joint collaborative representation and SVM with Decision Fusion (JSDF) [61], Probabilistic-Kernel Collaborative Representation Classification (PKCRC) [16], and Image Fusion and Recursive Filtering (IFRF) [17]. All methods are repeated ten times, where the mean accuracies and standard deviations are also reported.

B. Experimental Results

To evaluate the performance of our proposed ConGCN, ConGCN is compared with the above-mentioned baseline methods in both quantitative and qualitative aspects.

1) *Results on Indian Pines Dataset*: The quantitative results obtained by different methods on the *Indian Pines* dataset are summarized in Table II. We observe that the proposed ConGCN achieves the top-level performance among all the methods in terms of OA and kappa coefficient. The standard deviations are relatively small as well. Note that the proposed method achieves 100% accuracies on five land cover categories (*i.e.*, IDs = 4, 7, 8, 9, and 13), and can generally acquire stable and high classification accuracies on the remaining categories. Therefore, it is reasonable to infer that the proposed ConGCN is more stable and effective than the compared methods. The improvements of ConGCN over both CNN-based methods (*i.e.*, A²S²K and ASSMN) are even higher than 8% in terms of OA, which indicates the great potential of GCN in HSI classification. Moreover, it is notable that ConGCN performs better than three GCN-based methods (*i.e.*, SMR, MSSGU, and SGL), where the effectiveness of contextual information at both local and global levels is validated. The AA of our ConGCN is slightly lower than that of MSSGU, as MSSGU can adaptively incorporate features for various land cover categories from the graphs at different levels. Hence, MSSGU obtains better performance than ConGCN in several land cover categories, such as “Soybean-notill” (ID = 10) and “Stone-steel-towers” (ID = 16). Due to the instability of GAN during training [62], ADGAN has large standard deviations. Consequently, the four traditional HSI classification methods (namely, MFL, JSDF, PKCRC, and IFRF) achieve higher OAs, AAs, and kappa coefficients than ADGAN, indicating the effectiveness and stability of conventional pattern recognition methods. Although SSCL employs contrastive learning, its classification performance can still be unsatisfactory, especially in the land cover categories with IDs = 1, 4, 7, 9, 15, and 16. This is because SSCL only utilizes unlabeled examples to pre-train the encoder and simply

fine-tunes the network with few labeled examples. Different from SSCL, our proposed ConGCN utilizes the unlabeled data and the available class information, simultaneously, for model training. As a result, our proposed method outperforms SSCL on *Indian Pines* dataset.

Fig. 4 shows a visual comparison of the classification maps generated by different methods on the *Indian Pines* dataset, where the ground-truth map is exhibited in Fig. 4(b). The classification maps obtained by SMR (Fig. 4(c)), ASSMN (Fig. 4(h)), and MFL (Fig. 4(j)) suffer from pepper-noise-like mistakes within multiple areas. For instance, the middle parts of the classification maps obtained by SMR (Fig. 4(c)), ASSMN (Fig. 4(h)), and MFL (Fig. 4(j)) are highly confusing. Comparatively, the classification map of the proposed ConGCN method yields a smoother visual effect and shows fewer misclassifications than the compared methods.

2) *Results on University of Pavia Dataset*: Table III presents the quantitative results of different methods on the *University of Pavia* dataset. Similar to the results on *Indian Pines* dataset, in Table III, ConGCN outperforms the compared methods in terms of OA and kappa coefficient, which again validates the strength of our proposed contrastive learning-based graph convolution. Besides, the GCN-based methods (*i.e.*, SMR, MSSGU, and SGL) obtain higher OAs, AAs, and kappa coefficients than CNN-based methods (*i.e.*, A^2S^2K and ASSMN), which indicates the great potential of GCN in HSI classification. It is also notable that the performance of SMR on the *University of Pavia* dataset is better than that on the *Indian Pines* dataset. Since SMR can flexibly capture the variations around irregular boundaries with different convolutional kernels, the advantage of SMR becomes prominent on datasets containing various irregular boundaries, such as the *University of Pavia* dataset. Moreover, compared with the CNN-based methods, the proposed ConGCN outperforms the CNN-based methods (*i.e.*, A^2S^2K and ASSMN) with substantial margins (*i.e.*, 8.15% and 13.43%), which suggests that both spectral signatures and spatial relations captured by our ConGCN are more useful than the information characterized by the fixed convolutional kernels of CNN. The OAs of four traditional methods can reach 90% or higher, which confirms the good discriminability of conventional pattern recognition methods.

Fig. 5 visualizes the classification results generated by different methods on the *University of Pavia* dataset. As depicted in Fig. 5(n), the classification map of our proposed ConGCN is noticeably closer to the ground-truth map (Fig. 5(b)) than those of other methods, which is consistent with previous results in Table III. Besides, A^2S^2K (Fig. 5(g)) and ASSMN (Fig. 5(h)), which use the fixed convolutional kernels, produce more errors than ConGCN. In the classification map of ADGAN (Fig. 5(i)), most of the pixels are misclassified as the same land cover category, which illustrates the reason for ADGAN's poor OA. It is also notable that large numbers of pixels in the classification map of SSCL (Fig. 5(f)) are misclassified. It indicates that the performance of simply using the traditional paradigm of contrastive learning is far from satisfactory, especially with few labeled examples.

3) *Results on Salinas Dataset*: The experimental results of different methods on the *Salinas* dataset are presented in

Table IV. It is apparent that the performances of nearly all the methods on the *Salinas* dataset are better than those on the *Indian Pines* dataset and the *University of Pavia* dataset. The reason might be that the boundaries in the *Salinas* dataset are more regular than those in the *Indian Pines* and the *University of Pavia* datasets. As a result, the regions of the *Salinas* dataset are more distinguishable than those of the *Indian Pines* and the *University of Pavia* datasets. Although the proposed ConGCN is in the second place, it is only 0.18% lower than MSSGU in terms of OA. It is noticeable that MSSGU, SGL, and our proposed ConGCN all achieve good classification results, outperforming the CNN-based baseline methods (*i.e.*, A^2S^2K and ASSMN) regarding OA, AA, and kappa coefficient, respectively. It verifies the effectiveness of GCN-based methods in HSI classification. It is noted that the OA of IFRF is slightly lower than that of ConGCN. IFRF is a filter-based method, which utilizes recursive filtering to explore spatial information. Different from IFRF, our proposed method jointly incorporates contextual information at different spatial levels by employing localized and hierarchical graph convolution, simultaneously, thus revealing better representation ability than IFRF.

Fig. 6 visualizes the classification results generated by different methods. The classification maps obtained by SMR (Fig. 6(c)), SSCL (Fig. 6(f)), ASSMN (Fig. 6(h)), and MFL (Fig. 6(j)) suffer from noise-like mistakes within multiple areas. On the contrary, it can be observed that the classification map of our proposed ConGCN (Fig. 6(n)) is less noisy than those of other methods, which is consistent with the results listed in Table IV.

4) *Results on Houston University Dataset*: Table V shows the classification results obtained by different methods on the *Houston University* dataset. We can observe that the proposed ConGCN outperforms all the compared methods by a substantial margin in terms of OA, AA, and kappa coefficient. In addition, the standard deviations of ConGCN are relatively small as well. Another notable fact is that our proposed ConGCN outperforms other methods in seven land cover categories, which reveals the effectiveness of our method. Furthermore, our proposed ConGCN obtains OA increments of 6.72%, 2.58%, and 13.90% in comparison with the three GCN-based methods, namely SMR, MSSGU, and SGL, respectively. It can be inferred that the semi-supervised contrastive loss and the graph generative loss designed by our method are beneficial to improving the discriminative ability of the GCN-based methods. Meanwhile, we can see that although A^2S^2K captures discriminative spectral-spatial features with the spectral attention mechanism, its OA is still lower than that of ConGCN. We speculate that the supervision signals extracted from the spectral-spatial information of HSI are more dominant in improving the model performance when compared with the spectral attention mechanism employed by A^2S^2K . Consequently, our proposed ConGCN achieves stable and encouraging performance.

The classification results produced by different methods are visualized in Fig. 7, where the zoomed-in regions are denoted by red boxes. As can be seen, there are noticeable errors in the classification maps of other methods. By contrast, our proposed ConGCN (Fig. 7(n)) achieves more precise

TABLE II

PER-CLASS ACCURACIES, OAS, AAS (%), AND KAPPA COEFFICIENTS ACHIEVED BY DIFFERENT METHODS ON *Indian Pines* DATASET. THE BEST AND SECOND BEST RECORDS IN EACH ROW ARE **BOLDED** AND UNDERLINED, RESPECTIVELY.

ID	SMR [58]	MSSGU [33]	SGL [59]	SSCL [42]	A ² S ² K [24]	ASSMN [25]	ADGAN [22]	MFL [60]	JSDF [61]	PKCRC [16]	IFRF [17]	ConGCN
1	98.91±3.26	100.00±0.00	100.00±0.00	00.00±0.00	79.31±18.46	100.00±0.00	100.00±0.00	98.06±0.58	100.00±0.00	100.00±0.00	77.49±35.90	98.75±3.75
2	63.81±13.64	91.69±1.52	89.08±4.56	43.62±4.44	87.85±3.40	78.83±3.79	68.59±10.54	74.72±0.66	90.75±3.19	75.49±5.15	93.25±3.40	92.07±1.55
3	69.32±15.02	98.35±0.60	90.00±3.24	32.84±9.89	86.00±6.73	83.78±6.61	58.80±11.33	82.14±0.70	77.84±3.81	78.91±13.08	84.41±9.04	97.50±0.64
4	92.36±11.51	98.13±0.56	97.10±4.43	0.93±2.00	86.14±7.12	94.49±1.15	95.02±2.98	93.60±0.55	99.86±0.33	100.00±0.00	84.68±9.64	100.00±0.00
5	82.88±9.25	95.92±0.81	97.75±1.73	29.15±17.33	91.95±2.83	90.84±1.57	75.74±9.50	92.54±0.43	87.20±2.73	91.39±4.27	94.42±6.21	94.50±1.79
6	87.77±6.99	99.84±0.23	99.30±0.42	69.05±9.90	95.36±1.53	90.56±1.75	91.54±9.22	98.40±0.27	98.54±0.28	99.34±0.78	96.85±2.18	98.99±0.04
7	97.14±8.57	100.00±0.00	0.00±0.00	0.00±0.00	47.39±9.54	100.00±0.00	100.00±0.00	97.28±0.45	100.00±0.00	96.92±3.77	62.99±29.26	100.00±0.00
8	95.29±8.04	100.00±0.00	100.00±0.00	88.28±13.10	99.88±0.28	100.00±0.00	94.84±13.74	99.82±0.05	99.80±0.31	100.00±0.00	100.00±0.00	100.00±0.00
9	98.50±4.50	100.00±0.00	100.00±0.00	0.00±0.00	0.00±0.00	30.17±5.98	100.00±0.00	100.00±0.00	100.00±0.00	100.00±0.00	54.22±23.22	100.00±0.00
10	82.90±12.13	96.26±1.52	90.50±6.12	48.85±14.17	67.29±7.01	89.68±3.23	82.00±5.35	84.59±0.53	89.99±4.24	88.20±5.64	87.84±5.35	93.57±2.86
11	59.46±10.33	91.54±0.78	94.76±3.50	77.03±4.96	97.21±1.51	76.62±3.82	65.56±0.75	83.73±0.39	76.75±5.12	95.53±2.00	97.12±1.19	
12	79.45±16.60	98.47±0.51	94.33±2.67	37.67±13.70	83.37±8.30	91.72±3.10	83.53±7.38	83.68±0.72	87.10±2.82	93.80±1.93	89.44±5.78	97.57±0.87
13	94.63±6.37	100.00±0.00	99.09±0.38	47.02±39.63	85.05±4.42	100.00±0.00	100.00±0.00	99.20±0.06	99.89±0.36	100.00±0.00	91.99±4.87	100.00±0.00
14	93.91±4.44	99.98±0.04	99.84±0.24	78.35±8.32	99.43±0.35	94.01±2.02	91.17±6.65	96.80±0.40	97.21±2.78	93.30±2.29	99.30±0.63	99.83±0.02
15	62.62±15.17	99.77±0.36	99.58±0.42	12.56±11.33	87.97±5.28	98.46±1.19	92.89±0.99	97.86±0.20	99.58±0.68	95.62±5.26	92.33±4.26	99.41±0.08
16	96.67±6.84	100.00±0.00	100.00±0.00	1.94±3.81	85.43±4.50	100.00±0.00	99.05±1.05	98.72±0.35	100.00±0.00	100.00±0.00	96.59±1.32	87.14±2.18
OA	75.84±9.40	95.87±0.11	94.35±0.93	55.53±1.63	88.31±1.51	86.38±1.78	77.51±5.53	87.38±0.12	88.34±1.39	86.88±1.57	92.56±1.55	96.74±0.50
AA	84.73±8.30	98.12±0.09	84.46±0.42	35.46±3.18	81.86±1.38	93.06±1.00	87.42±3.36	92.57±0.10	94.03±0.55	93.31±1.25	87.58±3.02	97.28±0.29
kappa	72.87±10.33	95.28±0.13	93.53±1.06	48.47±2.03	86.76±1.67	84.51±2.02	74.98±5.93	85.64±0.14	86.80±1.55	85.09±1.81	91.51±1.74	96.27±0.57

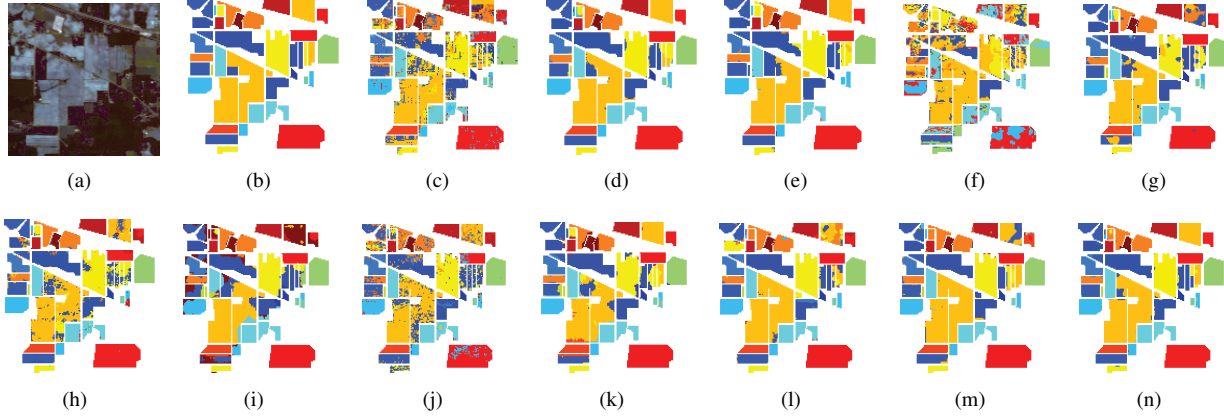


Fig. 4. Classification maps obtained by different methods on *Indian Pines* dataset. (a) False-color image. (b) Ground-truth map. (c) SMR. (d) MSSGU. (e) SGL. (f) SSCL. (g) A²S²K. (h) ASSMN. (i) ADGAN. (j) MFL. (k) JSDF. (l) PKCRC. (m) IFRF. (n) ConGCN (Proposed).

TABLE III

PER-CLASS ACCURACIES, OAS, AAS (%), AND KAPPA COEFFICIENTS ACHIEVED BY DIFFERENT METHODS ON *University of Pavia* DATASET. THE BEST AND SECOND BEST RECORDS IN EACH ROW ARE **BOLDED** AND UNDERLINED, RESPECTIVELY.

ID	SMR [58]	MSSGU [33]	SGL [59]	SSCL [42]	A ² S ² K [24]	ASSMN [25]	ADGAN [22]	MFL [60]	JSDF [61]	PKCRC [16]	IFRF [17]	ConGCN
1	96.96±1.89	98.14±0.72	88.26±3.06	96.94±1.76	94.25±2.75	78.33±3.30	49.97±20.68	94.45±0.25	82.40±4.07	96.69±3.22	85.15±7.06	93.11±2.43
2	82.00±6.11	82.90±2.30	97.24±1.45	97.90±1.90	97.92±2.08	74.97±1.80	33.82±23.16	90.17±0.65	90.76±3.74	92.57±7.68	98.83±0.53	96.55±1.87
3	95.21±2.60	100.00±0.00	94.19±2.64	14.89±16.14	72.27±11.87	81.14±6.84	70.07±35.81	85.05±0.54	86.71±4.14	94.07±6.85	83.46±4.72	97.24±1.83
4	94.73±3.47	98.44±0.45	92.76±1.97	42.87±19.21	78.73±5.59	97.76±1.06	54.79±24.08	93.31±0.28	92.88±2.16	91.63±4.96	85.76±7.41	93.91±0.25
5	99.03±1.48	100.00±0.00	99.30±0.82	87.00±13.48	99.92±0.02	99.98±0.03	91.10±25.17	99.38±0.02	100.00±0.00	100.00±0.00	99.50±0.74	98.80±0.15
6	99.79±0.36	100.00±0.00	99.80±0.51	9.43±7.15	81.74±7.58	90.76±3.69	58.62±31.24	93.31±0.20	94.30±4.55	99.38±1.04	91.21±3.12	100.00±0.00
7	97.59±5.41	100.00±0.00	99.31±0.23	14.21±12.56	81.40±9.44	98.43±1.26	85.29±29.34	99.39±0.04	96.62±3.37	100.00±0.00	84.24±6.12	99.12±0.44
8	88.79±14.78	99.48±0.97	94.07±2.12	81.36±14.61	70.44±6.86	89.38±1.92	48.79±31.33	85.30±0.53	94.69±3.74	98.79±1.60	74.96±4.86	94.76±1.93
9	99.09±1.47	99.86±0.11	99.67±0.00	2.30±6.87	95.60±4.33	99.87±0.18	90.08±7.88	99.76±0.02	99.56±0.36	99.89±0.00	66.16±12.01	82.81±3.20
OA	90.13±3.94	92.06±1.01	95.58±0.60	72.85±2.44	87.82±1.47	82.54±0.99	48.35±17.95	91.54±0.30	90.82±1.30	95.16±3.68	90.10±1.57	95.97±0.90
AA	94.80±3.11	97.65±0.26	96.07±0.47	49.66±3.58	85.81±1.82	90.07±1.20	64.73±16.71	93.35±0.10	93.10±0.65	97.00±1.28	85.48±1.86	95.14±0.57
kappa	87.51±4.86	89.81±1.26	94.17±0.78	61.18±3.55	84.32±1.88	77.87±1.20	42.94±17.63	88.98±0.38	88.02±1.62	93.73±4.69	87.04±2.03	94.69±1.17

classification results than other methods, which confirms the advantage of our method.

C. Impact of the Number of Labeled Examples

In this subsection, OAs of the proposed ConGCN and baseline methods under different numbers of labeled examples are shown in Fig. 8. We vary the number of labeled examples per class from 5 to 30 with an interval of 5 and report the OAs gained by all the methods on six datasets (*i.e.*, *Indian Pines*, *University of Pavia*, *Salinas*, *Houston University*, *WHU-Hi-HanChuan*, and *WHU-Hi-HongHu* datasets). As observed in Fig. 8, the classification performances of all other methods except ADGAN can be generally improved by increasing

the number of labeled examples. Due to the instability of GAN during training [62], the OAs of ADGAN could drop significantly on the *Indian Pines* (Fig. 8(a)), *University of Pavia* (Fig. 8(b)), *Salinas* (Fig. 8(c)), and *Houston University* (Fig. 8(d)) datasets even when the number of labeled examples increases. Thanks to the exploration of the supervision signals from both spectral and spatial aspects of HSI, our ConGCN still achieves relatively high OAs even if the labeled examples are quite limited (*i.e.*, five or ten labeled examples per class), which suggests the good stability of ConGCN in HSI classification. The corresponding AAs and kappa coefficients under different numbers of labeled examples are presented in

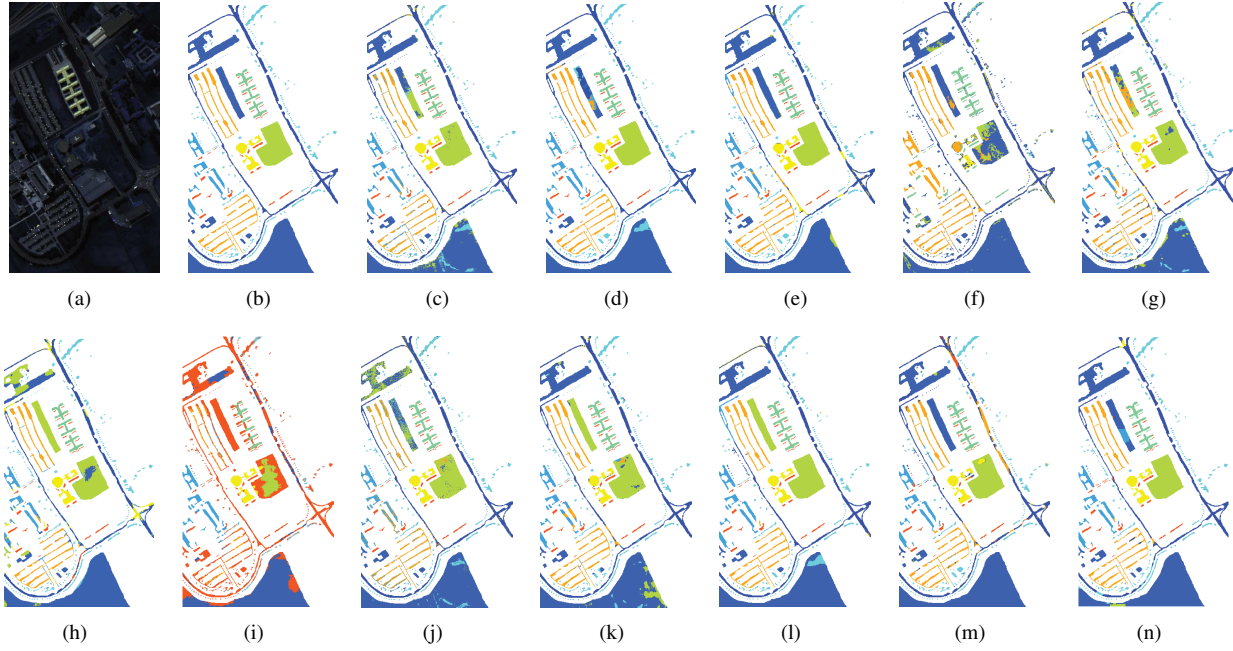


Fig. 5. Classification maps obtained by different methods on *University of Pavia* dataset. (a) False-color image. (b) Ground-truth map. (c) SMR. (d) MSSGU. (e) SGL. (f) SSCL. (g) A^2S^2K . (h) ASSMN. (i) ADGAN. (j) MFL. (k) JSDF. (l) PKCRC. (m) IFRF. (n) ConGCN (Proposed).

TABLE IV

PER-CLASS ACCURACIES, OAS, AAS (%), AND KAPPA COEFFICIENTS ACHIEVED BY DIFFERENT METHODS ON *Salinas* DATASET. THE BEST AND SECOND BEST RECORDS IN EACH ROW ARE **BOLDED** AND UNDERLINED, RESPECTIVELY.

ID	SMR [58]	MSSGU [33]	SGL [59]	SSCL [42]	A^2S^2K [24]	ASSMN [25]	ADGAN [22]	MFL [60]	JSDF [61]	PKCRC [16]	IFRF [17]	ConGCN
1	99.82±0.31	100.00±0.00	100.00±0.00	81.57±13.21	100.00±0.00	97.68±6.17	95.36±6.40	99.63±0.07	100.00±0.00	100.00±0.00	99.98±0.06	100.00±0.00
2	99.53±0.73	<u>99.99±0.03</u>	100.00±0.00	81.56±8.56	99.98±0.05	99.02±0.46	54.19±42.34	99.34±0.06	100.00±0.00	<u>100.00±0.01</u>	100.00±0.00	100.00±0.00
3	99.74±0.21	100.00±0.00	100.00±0.00	43.48±10.02	99.98±0.02	99.57±0.39	85.70±20.43	99.77±0.03	100.00±0.00	100.00±0.00	99.79±0.26	100.00±0.00
4	99.86±0.28	99.88±0.07	98.15±0.85	91.79±14.35	<u>99.25±0.42</u>	99.87±0.14	95.09±2.96	98.88±0.07	99.93±0.09	<u>99.94±0.03</u>	96.89±1.44	98.50±0.82
5	97.23±1.18	99.50±0.17	98.36±0.05	95.72±1.36	99.52±0.28	98.62±0.86	92.34±14.98	98.72±0.04	<u>99.77±0.31</u>	99.20±0.16	99.68±0.44	97.58±0.60
6	99.53±1.04	100.00±0.00	100.00±0.00	98.00±2.05	<u>99.99±0.02</u>	99.93±0.10	83.01±28.61	99.18±0.11	100.00±0.00	99.99±0.01	<u>99.99±0.02</u>	99.81±0.07
7	99.81±0.16	100.00±0.01	99.89±0.00	99.26±0.59	<u>99.95±0.08</u>	99.81±0.10	96.40±3.93	98.61±0.12	99.99±0.01	100.00±0.00	99.66±0.16	99.94±0.01
8	86.35±7.29	97.65±0.70	<u>98.52±0.39</u>	79.63±5.01	88.89±2.12	77.54±7.53	35.07±36.66	76.57±0.71	87.79±4.89	85.09±7.50	99.06±1.39	98.33±1.16
9	99.37±0.63	100.00±0.00	100.00±0.00	97.57±2.33	99.49±0.05	99.06±0.38	92.68±16.75	99.01±0.05	99.67±0.33	100.00±0.00	99.95±0.13	100.00±0.00
10	97.19±1.20	99.47±0.10	97.98±1.70	66.90±15.77	98.74±0.68	97.04±1.87	96.82±2.36	93.10±0.30	96.53±2.55	97.75±0.74	<u>99.53±0.62</u>	99.28±0.68
11	97.05±1.93	100.00±0.00	97.86±2.27	40.83±36.55	100.00±0.00	98.85±1.40	99.03±0.03	96.81±0.30	<u>99.76±0.21</u>	98.15±1.83	99.17±0.30	99.74±0.09
12	100.00±0.00	99.87±0.17	99.74±0.00	86.39±15.94	<u>99.93±0.13</u>	99.76±0.38	93.63±3.82	98.84±0.20	100.00±0.00	100.00±0.00	99.66±0.36	98.26±0.71
13	99.93±0.17	100.00±0.00	98.70±0.06	28.77±35.22	<u>99.95±0.08</u>	99.40±0.26	95.49±3.60	99.38±0.08	100.00±0.00	98.89±0.45	97.78±1.40	97.58±0.47
14	98.91±0.69	99.81±0.23	94.86±1.09	68.89±26.04	<u>99.95±0.07</u>	98.31±1.32	98.41±1.21	96.20±0.32	98.71±0.72	99.50±0.63	96.98±1.92	98.86±0.46
15	77.41±9.95	99.95±0.07	98.96±0.36	61.92±10.33	85.44±4.44	89.34±7.49	94.48±4.49	78.85±0.56	81.86±5.26	85.31±10.71	94.27±2.92	99.63±0.29
16	99.30±0.51	100.00±0.00	98.62±0.90	42.50±23.01	<u>99.57±0.67</u>	97.87±0.59	96.11±0.52	99.69±0.06	98.99±0.63	99.44±0.38	99.87±0.19	100.00±0.00
OA	93.60±0.93	99.43±0.14	99.08±0.11	78.34±3.52	95.44±0.54	93.17±1.56	78.31±9.20	91.20±0.13	94.67±0.77	94.63±1.74	98.69±0.50	99.25±0.29
AA	96.94±0.37	99.76±0.05	98.85±0.18	72.80±5.02	98.17±0.22	96.98±0.94	87.74±4.92	95.79±0.04	97.69±0.34	97.70±0.64	98.89±0.25	99.22±0.19
kappa	92.87±1.03	99.37±0.16	98.97±0.12	75.78±3.97	94.91±0.60	92.41±1.73	76.52±9.84	90.21±0.14	94.06±0.85	94.03±1.94	98.54±0.55	99.17±0.33

TABLE V

PER-CLASS ACCURACIES, OAS, AAS (%), AND KAPPA COEFFICIENTS ACHIEVED BY DIFFERENT METHODS ON *Houston University* DATASET. THE BEST AND SECOND BEST RECORDS IN EACH ROW ARE **BOLDED** AND UNDERLINED, RESPECTIVELY.

ID	SMR [58]	MSSGU [33]	SGL [59]	SSCL [42]	A^2S^2K [24]	ASSMN [25]	ADGAN [22]	MFL [60]	JSDF [61]	PKCRC [16]	IFRF [17]	ConGCN
1	92.64±3.13	98.35±2.46	89.13±6.46	78.18±8.63	97.80±1.49	94.52±2.79	60.27±24.21	91.00±0.90	97.41±1.21	79.00±1.38	81.73±6.26	97.79±0.92
2	98.21±1.01	91.81±2.24	75.79±6.67	42.96±11.79	98.53±1.02	97.46±2.53	23.69±16.97	94.97±0.62	99.48±0.25	75.80±1.37	74.54±4.78	97.35±0.59
3	97.14±1.97	99.60±0.34	99.60±0.04	95.91±1.20	99.76±0.48	98.22±0.29	94.49±6.77	99.74±0.01	99.88±0.22	100.00±0.00	93.65±2.34	98.25±0.32
4	98.28±1.78	99.68±0.48	75.16±2.67	66.31±7.73	97.00±1.08	92.75±7.85	42.58±16.45	93.14±0.45	98.22±2.80	82.89±1.77	70.83±5.22	99.74±0.52
5	97.75±1.01	100.00±0.00	99.05±0.47	70.72±13.86	98.55±0.94	97.08±1.26	53.16±16.55	98.36±0.15	100.00±0.00	88.53±2.76	92.96±2.28	99.79±0.33
6	98.58±1.23	99.63±0.65	96.47±2.54	10.62±15.89	98.70±1.81	98.07±1.06	91.83±7.87	97.24±0.40	99.32±1.09	79.86±3.54	74.66±10.71	97.29±0.00
7	92.93±2.78	95.33±1.36	69.51±6.61	64.06±10.15	94.74±3.38	86.52±5.93	57.26±33.71	88.02±0.52	91.93±4.91	85.85±4.41	81.42±2.77	98.18±0.43
8	81.22±3.26	90.30±2.88	67.83±5.24	19.08±10.07	<u>95.53±5.09</u>	73.38±3.93	31.79±11.21	64.28±0.71	68.82±6.16	51.28±8.90	79.36±7.30	97.75±1.38
9	85.01±4.59	90.66±3.00	75.73±4.31	67.63±10.58	<u>92.19±5.37</u>	72.18±7.57	26.59±15.06	67.91±0.57	69.47±8.56	86.34±2.44	90.30±4.09	97.77±1.28
10	90.37±5.50	100.00±0.00	97.14±7.22	29.60±15.16	83.72±2.76	82.47±5.35	27.29±23.47	87.64±0.95	85.63±9.32	70.90±19.42	86.09±3.79	100.00±0.00
11	91.74±7.04	99.99±0.02	94.91±2.77	50.08±7.59	90.78±4.37	82.91±6.05	48.64±24.83	89.20±0.47	94.51±3.82	65.52±2.72	89.99±5.18	98.91±0.96
12	85.85±5.03	92.78±2.08	79.31±5.19	21.69±9.27	91.31±6.98	76.80±7.85	73.49±27.32	77.65±0.46	84.33±5.33	52.08±6.43	91.08±3.70	99.45±1.28
13	83.37±7.43	86.76±2.48	92.31±2.84	19.68±14.86	96.59±3.49	70.46±8.76	68.81±17.97	80.76±0.40	98.10±1.28	78.81±5.95	75.39±10.54	98.69±2.00
14	96.21±8.18	100.00±0.00	98.45±1.02	69.96±12.94	100.00±0.00	98.94±1.07	90.29±8.00	98.01±0.29	100.00±0.00	100.00±0.00	88.34±3.31	99.38±1.86
15	99.29±0.85	99.99±0.04	96.81±0.45	74.38±11.62	99.13±0.72	98.70±0.96	93.60±6.11	98.47±0.11	99.86±0.36	97.90±0.31	91.22±4.15	98.19±0.32
OA	91.89±1.93	96.03±0.52	84.71±1.28	52.69±2.23	94.37±0.74	86.60±3.33	51.57±9.80	86.66±0.13	90.51±0.95	76.98±1.41	83.96±1.11	98.61±0.37
AA	92.57±1.96	<u>96.33±0.45</u>	87.15±1.04	52.06±2.82	95.62±0.46	88.03±3.02	58.92±8.97	88.43±0.11	92.46±0.75	79.65±1.31	84.10±1.34	98.57±0.41
kappa	91.22±2.09	95.71±0.56	83.49±1.38	48.86±2.40	93.90±0.80	85.50±3.60	48.34±10.36	85.56±0.14	89.74±1.03	75.07±1.53	82.66±1.20	98.49±0.40

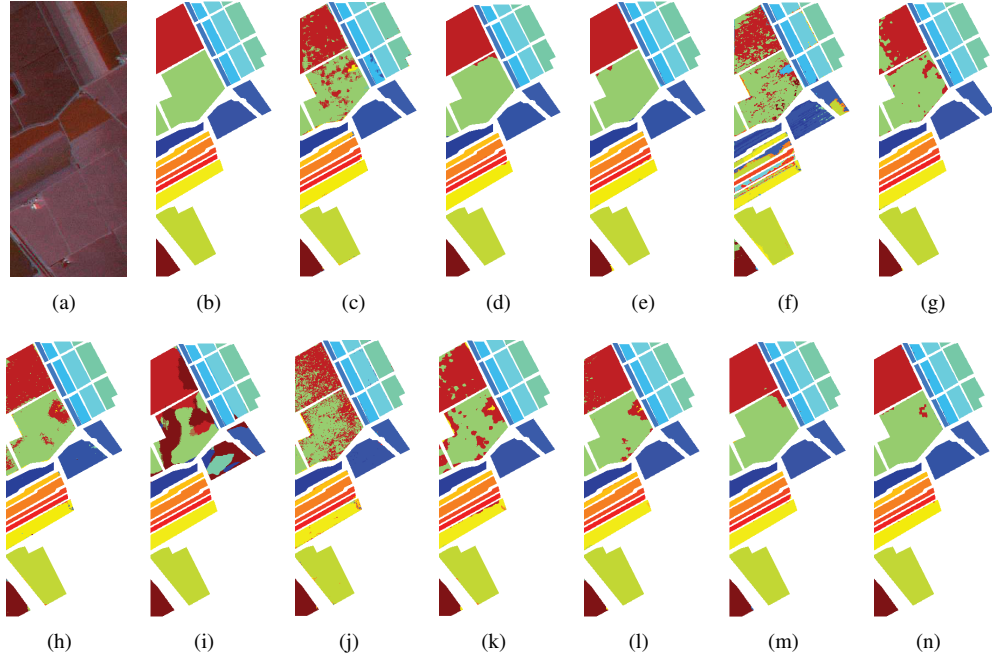


Fig. 6. Classification maps obtained by different methods on *Salinas* dataset. (a) False-color image. (b) Ground-truth map. (c) SMR. (d) MSSGU. (e) SGL. (f) SSCL. (g) A^2S^2K . (h) ASSMN. (i) ADGAN. (j) MFL. (k) JSDF. (l) PKCRC. (m) IFRF. (n) ConGCN (Proposed).

the appendix. In addition, to verify the effectiveness of the proposed ConGCN when given limited labeled examples, we only use 1, 2, 3, and 4 labeled examples per class for training, and the results are reported in the appendix.

D. Ablation Study

As mentioned in the introduction (Section I), the proposed ConGCN contains two parts that are critical for enriching the supervision signals from the spectral-spatial information of HSI, *i.e.*, the semi-supervised contrastive loss function and the graph generative loss function. We use the four datasets (*i.e.*, *Indian Pines*, *University of Pavia*, *Salinas*, and *Houston University* datasets) to shed light on the contributions of these two components, where the number of labeled pixels per class is kept identical to the above experiments in Section VII-B. Every time we report the OA, AA, and kappa coefficient obtained by ConGCN without one of the aforementioned loss functions. For simplicity, “w/o CLoss” and “w/o GLoss” indicate the reduced models by removing the contrastive loss function \mathcal{L}_{ssc} and the graph generative loss \mathcal{L}_{g^2} , respectively. In addition, we also investigate the effectiveness of the spatial-level and spectral-level graph augmentation. To be concrete, we utilize “w/o SpaAug” and “w/o SpeAug” to indicate the reduced models that remove the spatial-level graph augmentation and the spectral-level graph augmentation, respectively. Furthermore, we utilize “w/o CGSS” to indicate the reduced model that removes the semi-supervised contrastive loss, graph generative loss, spatial-level graph augmentation, and spectral-level graph augmentation, simultaneously. Concretely, Table VI, Table VII, Table VIII, and Table IX exhibit the comparative results, respectively. It is apparent that the OA will decline when any one of the aforementioned components is removed. Meanwhile, the

TABLE VI

OAS, AAS (%), AND KAPPA COEFFICIENTS ACHIEVED BY DIFFERENT SETTINGS ON *Indian Pines* DATASET. THE BEST AND SECOND BEST RECORDS IN EACH ROW ARE **BOLDED** AND UNDERLINED, RESPECTIVELY.

metrics	w/o CLoss	w/o GLoss	w/o SpaAug	w/o SpeAug	w/o CGSS	ConGCN
OA	96.44±0.55	96.46±0.68	<u>96.58±0.82</u>	96.56±0.68	95.78±1.33	96.74±0.50
AA	97.18±0.33	97.28±0.37	<u>97.25±0.43</u>	97.25±0.36	96.75±0.92	97.28±0.29
kappa	95.92±0.63	95.95±0.78	<u>96.09±0.93</u>	96.06±0.77	95.17±1.51	96.27±0.57

TABLE VII

OAS, AAS (%), AND KAPPA COEFFICIENTS ACHIEVED BY DIFFERENT SETTINGS ON *University of Pavia* DATASET. THE BEST AND SECOND BEST RECORDS IN EACH ROW ARE **BOLDED** AND UNDERLINED, RESPECTIVELY.

metrics	w/o CLoss	w/o GLoss	w/o SpaAug	w/o SpeAug	w/o CGSS	ConGCN
OA	95.05±1.13	95.32±1.54	95.37±1.62	<u>95.79±1.64</u>	94.62±1.36	95.97±0.90
AA	94.95±0.88	95.01±0.71	95.70±0.39	95.56±0.65	95.37±0.45	95.14±0.57
kappa	93.51±1.47	93.86±1.99	93.94±2.06	<u>94.48±2.09</u>	92.97±1.74	94.69±1.17

reduced model, *i.e.*, “w/o CGSS”, obtains the lowest OA on each dataset. It reveals that each component makes an essential contribution to boosting the classification performance. We can also observe that the reduced model “w/o GLoss” consistently achieves higher OA, AA, and kappa coefficient than “w/o CLoss” on each dataset, which validates that the semi-supervised contrastive loss makes a greater contribution than the generative loss to performance improvement.

VIII. CONCLUSION

In this paper, we propose a ConGCN algorithm for HSI classification. To improve feature representation ability, we explore the supervision signals based on the spectral and spatial information of HSI. Specifically, we devise a semi-supervised contrastive loss to exploit the supervision contained in the spectral signatures of image regions. Meanwhile, we develop a graph generative loss to explore supplementary supervision



Fig. 7. Classification maps obtained by different methods on *Houston University* dataset. (a) False-color image. (b) Ground-truth map. (c) SMR. (d) MSSGU. (e) SGL. (f) SSCL. (g) A²S²K. (h) ASSMN. (i) ADGAN. (j) MFL. (k) JSDF. (l) PKCRC. (m) IFRF. (n) ConGCN (Proposed). In (a)–(n), zoomed-in views of the regions are denoted by red boxes.

TABLE VIII

OAs, AAs (%), AND KAPPA COEFFICIENTS ACHIEVED BY DIFFERENT SETTINGS ON *Salinas* DATASET. THE BEST AND SECOND BEST RECORDS IN EACH ROW ARE **BOLDED** AND UNDERLINED, RESPECTIVELY.

metrics	w/o CLoss	w/o GLoss	w/o SpaAug	w/o SpeAug	w/o CGSS	ConGCN
OA	97.80±4.06	98.55±1.35	<u>99.09±0.31</u>	99.02±0.78	97.53±4.81	99.25±0.29
AA	98.50±2.06	98.90±0.74	<u>99.20±0.13</u>	99.07±0.42	98.59±1.43	99.22±0.19
kappa	97.56±4.48	98.39±1.50	<u>98.99±0.35</u>	98.91±0.86	97.28±5.29	99.17±0.33

TABLE IX

OAs, AAs (%), AND KAPPA COEFFICIENTS ACHIEVED BY DIFFERENT SETTINGS ON *Houston University* DATASET. THE BEST AND SECOND BEST RECORDS IN EACH ROW ARE **BOLDED** AND UNDERLINED, RESPECTIVELY.

metrics	w/o CLoss	w/o GLoss	w/o SpaAug	w/o SpeAug	w/o CGSS	ConGCN
OA	97.99±2.06	98.32±0.71	<u>98.53±0.34</u>	98.48±0.41	96.90±1.93	98.61±0.37
AA	97.93±2.25	98.33±0.69	<u>98.53±0.29</u>	98.49±0.38	96.83±2.04	98.57±0.41
kappa	97.82±2.22	98.18±0.77	<u>98.41±0.37</u>	98.36±0.44	96.64±2.09	98.49±0.40

signals from the spatial relations among image regions. Last but not least, we devise an adaptive graph augmentation technique via incorporating the spectral-spatial priors to boost the performance of contrastive learning. As a consequence,

the expressive power of the generated representation can be enhanced, which leads to the improved classification results. Experimental results on six real-world HSI datasets validate the effectiveness of our proposed ConGCN.

REFERENCES

- [1] S. Wan, C. Gong, P. Zhong, B. Du, L. Zhang, and J. Yang, “Multiscale dynamic graph convolutional network for hyperspectral image classification,” *IEEE Trans. Geosci. Remote Sens.*, vol. 58, no. 5, pp. 3162–3177, May 2020.
- [2] S. Wan, C. Gong, P. Zhong, S. Pan, G. Li, and J. Yang, “Hyperspectral image classification with context-aware dynamic graph convolutional network,” *IEEE Trans. Geosci. Remote Sens.*, vol. 59, no. 1, pp. 597–612, Jan. 2021.
- [3] S. Wan, S. Pan, P. Zhong, X. Chang, J. Yang, and C. Gong, “Dual interactive graph convolutional networks for hyperspectral image classification,” *IEEE Trans. Geosci. Remote Sens.*, early access, May 10, 2021, doi:[10.1109/TGRS.2021.3075223](https://doi.org/10.1109/TGRS.2021.3075223).
- [4] L. Mou, X. Lu, X. Li, and X. X. Zhu, “Nonlocal graph convolutional networks for hyperspectral image classification,” *IEEE Trans. Geosci. Remote Sens.*, vol. 58, no. 12, pp. 8246–8257, Dec. 2020.
- [5] J. Bai, B. Ding, Z. Xiao, L. Jiao, H. Chen, and A. C. Regan, “Hyperspectral image classification based on deep attention graph convolutional network,” *IEEE Trans. Geosci. Remote Sens.*, early access, Mar. 25, 2021, doi:[10.1109/TGRS.2021.3066485](https://doi.org/10.1109/TGRS.2021.3066485).

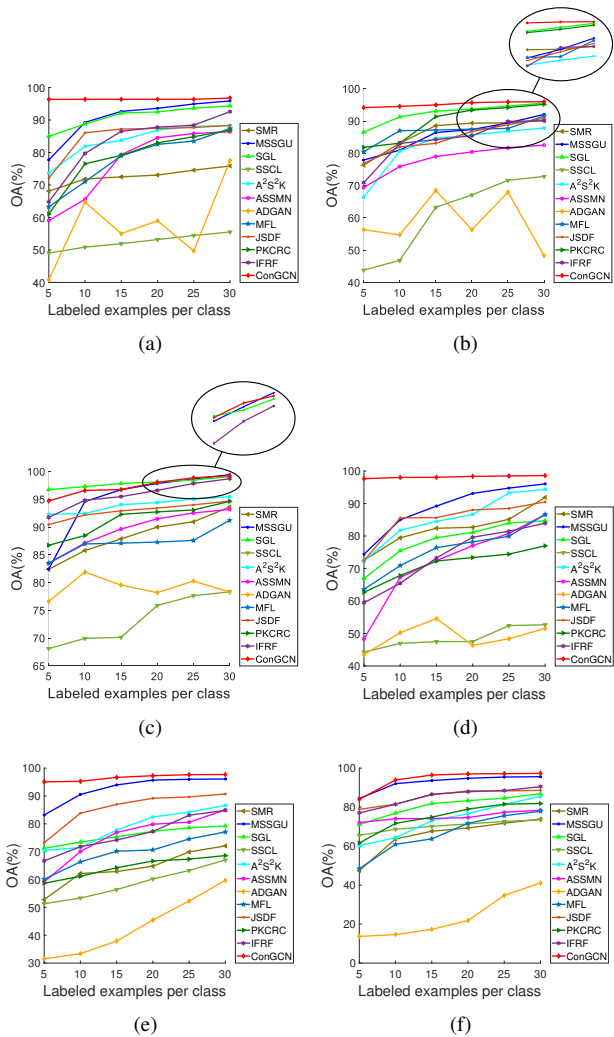


Fig. 8. OAs of various methods under different numbers of labeled examples per class. (a) Indian Pines dataset. (b) University of Pavia dataset. (c) Salinas dataset. (d) Houston University dataset. (e) WHU-Hi-HanChuan dataset. (f) WHU-Hi-HongHu dataset.

- [6] X. He, Y. Chen, and P. Ghamisi, “Dual graph convolutional network for hyperspectral image classification with limited training samples,” *IEEE Trans. Geosci. Remote Sens.*, early access, Mar. 8, 2021, doi:10.1109/TGRS.2021.3061088.
- [7] Y. Zhang, T. Wang, S. Mei, and Q. Du, “Subpixel mapping of hyperspectral images using a labeled-unlabeled hybrid endmember library and abundance optimization,” *IEEE J. Sel. Topics Appl. Earth Observ. Remote Sens.*, vol. 13, pp. 5036–5047, Jul. 2020.
- [8] B. Deng, S. Jia, and D. Shi, “Deep metric learning-based feature embedding for hyperspectral image classification,” *IEEE Trans. Geosci. Remote Sens.*, vol. 58, no. 2, pp. 1422–1435, Feb. 2020.
- [9] F. Xie, Q. Gao, C. Jin, and F. Zhao, “Hyperspectral image classification based on superpixel pooling convolutional neural network with transfer learning,” *Remote Sens.*, vol. 13, no. 5, pp. 1–16, Mar. 2021.
- [10] S. Wan, S. Pan, S. Zhong, J. Yang, J. Yang, Y. Zhan, and C. Gong, “Multi-level graph learning network for hyperspectral image classification,” *Pattern Recognit.*, vol. 129, p. 108705, Sep. 2022.
- [11] T. Chen, S. Kornblith, M. Norouzi, and G. Hinton, “A simple framework for contrastive learning of visual representations,” in *Proc. Int. Conf. Mach. Learn. (ICML)*, Jul. 2020, pp. 1597–1607.
- [12] K. He, H. Fan, Y. Wu, S. Xie, and R. Girshick, “Momentum contrast for unsupervised visual representation learning,” in *Proc. IEEE/CVF Conf. Comput. Vis. Pattern Recognit. (CVPR)*, Jun. 2020, pp. 9729–9738.
- [13] S. Wan, S. Pan, J. Yang, and C. Gong, “Contrastive and generative graph convolutional networks for graph-based semi-supervised learning,” *arXiv:2009.07111*, 2020. [Online]. Available: <https://arxiv.org/abs/2009.07111>
- [14] S. Wan, Y. Zhan, L. Liu, B. Yu, S. Pan, and C. Gong, “Contrastive graph poisson networks: Semi-supervised learning with extremely limited labels,” in *Proc. Conf. Adv. Neural Inf. Process. Syst. (NeurIPS)*, 2021, pp. 6316–6327.
- [15] G. Camps-Valls and L. Bruzzone, “Kernel-based methods for hyperspectral image classification,” *IEEE Trans. Geosci. Remote Sens.*, vol. 43, no. 6, pp. 1351–1362, Jun. 2005.
- [16] J. Liu, Z. Wu, J. Li, A. Plaza, and Y. Yuan, “Probabilistic-kernel collaborative representation for spatial-spectral hyperspectral image classification,” *IEEE Trans. Geosci. Remote Sens.*, vol. 54, no. 4, pp. 2371–2384, Apr. 2016.
- [17] X. Kang, S. Li, and J. A. Benediktsson, “Feature extraction of hyperspectral images with image fusion and recursive filtering,” *IEEE Trans. Geosci. Remote Sens.*, vol. 52, no. 6, pp. 3742–3752, Jun. 2014.
- [18] L. Ma, M. M. Crawford, and J. Tian, “Local manifold learning-based k -nearest-neighbor for hyperspectral image classification,” *IEEE Trans. Geosci. Remote Sens.*, vol. 48, no. 11, pp. 4099–4109, Nov. 2010.
- [19] J. Peng, Y. Zhou, and C. P. Chen, “Region-kernel-based support vector machines for hyperspectral image classification,” *IEEE Trans. Geosci. Remote Sens.*, vol. 53, no. 9, pp. 4810–4824, Sep. 2015.
- [20] X. Zhang, Z. Gao, L. Jiao, and H. Zhou, “Multifeature hyperspectral image classification with local and nonlocal spatial information via Markov random field in semantic space,” *IEEE Trans. Geosci. Remote Sens.*, vol. 56, no. 3, pp. 1409–1424, Mar. 2017.
- [21] J. Feng, N. Zhao, R. Shang, X. Zhang, and L. Jiao, “Self-supervised divide-and-conquer generative adversarial network for classification of hyperspectral images,” *IEEE Trans. Geosci. Remote Sens.*, early access, Aug. 29, 2022, doi:10.1109/TGRS.2022.3202908.
- [22] J. Wang, F. Gao, J. Dong, and Q. Du, “Adaptive dropblock-enhanced generative adversarial networks for hyperspectral image classification,” *IEEE Trans. Geosci. Remote Sens.*, vol. 59, no. 6, pp. 5040–5053, Jun. 2021.
- [23] Y. Chen, H. Jiang, C. Li, X. Jia, and P. Ghamisi, “Deep feature extraction and classification of hyperspectral images based on convolutional neural networks,” *IEEE Trans. Geosci. Remote Sens.*, vol. 54, no. 10, pp. 6232–6251, Oct. 2016.
- [24] S. K. Roy, S. Manna, T. Song, and L. Bruzzone, “Attention-based adaptive spectral-spatial kernel ResNet for hyperspectral image classification,” *IEEE Trans. Geosci. Remote Sens.*, vol. 59, no. 9, pp. 7831–7843, Sep. 2021.
- [25] D. Wang, B. Du, L. Zhang, and Y. Xu, “Adaptive spectral-spatial multiscale contextual texture feature extraction for hyperspectral image classification,” *IEEE Trans. Geosci. Remote Sens.*, vol. 59, no. 3, pp. 2461–2477, Mar. 2021.
- [26] J. Feng, J. Chen, Q. Sun, R. Shang, X. Cao, X. Zhang, and L. Jiao, “Convolutional neural network based on bandwise-independent convolution and hard thresholding for hyperspectral band selection,” *IEEE Trans. Cybern.*, vol. 51, no. 9, pp. 4414–4428, Sep. 2021.
- [27] M. Gori, G. Monfardini, and F. Scarselli, “A new model for learning in graph domains,” in *Proc. Int. Joint Conf. Neural Netw. (IJCNN)*, 2005, pp. 729–734.
- [28] J. Bruna, W. Zaremba, A. Szlam, and Y. LeCun, “Spectral networks and locally connected networks on graphs,” *arXiv:1312.6203*, 2013. [Online]. Available: <https://arxiv.org/abs/1312.6203>
- [29] T. N. Kipf and M. Welling, “Semi-supervised classification with graph convolutional networks,” *arXiv:1609.02907*, 2016. [Online]. Available: <https://arxiv.org/abs/1609.02907>
- [30] W. L. Hamilton, R. Ying, and J. Leskovec, “Inductive representation learning on large graphs,” in *Proc. Conf. Adv. Neural Inf. Process. Syst. (NeurIPS)*, 2017, pp. 1025–1035.
- [31] A. Qin, Z. Shang, J. Tian, Y. Wang, T. Zhang, and Y. Y. Tang, “Spectral-spatial graph convolutional networks for semisupervised hyperspectral image classification,” *IEEE Geosci. Remote Sens. Lett.*, vol. 16, no. 2, pp. 241–245, Feb. 2019.
- [32] Q. Liu, L. Xiao, J. Yang, and Z. Wei, “CNN-enhanced graph convolutional network with pixel-and superpixel-level feature fusion for hyperspectral image classification,” *IEEE Trans. Geosci. Remote Sens.*, vol. 59, no. 10, pp. 8657–8671, Oct. 2021.
- [33] Q. Liu, L. Xiao, J. Yang, and Z. Wei, “Multilevel superpixel structured graph U-nets for hyperspectral image classification,” *IEEE Trans. Geosci. Remote Sens.*, early access, Sep. 24, 2021, doi:10.1109/TGRS.2021.3112586.
- [34] Y. Ding, X. Zhao, Z. Zhang, W. Cai, and N. Yang, “Multiscale graph sample and aggregate network with context-aware learning for hyper-

- spectral image classification,” *IEEE J. Sel. Topics Appl. Earth Observ. Remote Sens.*, vol. 14, pp. 4561–4572, Apr. 2021.
- [35] F. Guo, Z. Li, Z. Xin, X. Zhu, L. Wang, and J. Zhang, “Dual graph U-nets for hyperspectral image classification,” *IEEE J. Sel. Topics Appl. Earth Observ. Remote Sens.*, early access, Aug. 10, 2021, doi:10.1109/JSTARS.2021.3103744.
- [36] R. Liu, “Understand and improve contrastive learning methods for visual representation: A review,” *arXiv:2106.03259*, 2021. [Online]. Available: <https://arxiv.org/abs/2106.03259>
- [37] L. Kong, C. d. M. d’Autume, W. Ling, L. Yu, Z. Dai, and D. Yogatama, “A mutual information maximization perspective of language representation learning,” *arXiv:1910.08350*, 2019. [Online]. Available: <https://arxiv.org/abs/1910.08350>
- [38] A. Van den Oord, Y. Li, and O. Vinyals, “Representation learning with contrastive predictive coding,” *arXiv:1807.03748*, 2018. [Online]. Available: <https://arxiv.org/abs/1807.03748>
- [39] P. Velickovic, W. Fedus, W. L. Hamilton, P. Liò, Y. Bengio, and R. D. Hjelm, “Deep graph infomax,” in *Proc. Int. Conf. Learn. Represent. (ICLR)*, 2019, pp. 1–17.
- [40] Y. You, T. Chen, Y. Sui, T. Chen, Z. Wang, and Y. Shen, “Graph contrastive learning with augmentations,” in *Proc. Conf. Adv. Neural Inf. Process. Syst. (NeurIPS)*, 2020, pp. 5812–5823.
- [41] Z. Peng, W. Huang, M. Luo, Q. Zheng, Y. Rong, T. Xu, and J. Huang, “Graph representation learning via graphical mutual information maximization,” in *Proc. Web Conf. (WWW)*, Apr. 2020, pp. 259–270.
- [42] S. Hou, H. Shi, X. Cao, X. Zhang, and L. Jiao, “Hyperspectral imagery classification based on contrastive learning,” *IEEE Trans. Geosci. Remote Sens.*, early access, Dec. 28, 2021, doi:10.1109/TGRS.2021.3139099.
- [43] X. Hu, T. Li, T. Zhou, Y. Liu, and Y. Peng, “Contrastive learning based on transformer for hyperspectral image classification,” *Appl. Sci.*, vol. 11, no. 18, pp. 8670–8687, Sep. 2021.
- [44] R. Achanta, A. Shajii, K. Smith, A. Lucchi, P. Fua, and S. Süsstrunk, “Slic superpixels compared to state-of-the-art superpixel methods,” *IEEE Trans. Pattern Anal. Mach. Intell.*, vol. 34, no. 11, pp. 2274–2282, Nov. 2012.
- [45] Y. Zhu, Y. Xu, F. Yu, Q. Liu, S. Wu, and L. Wang, “Graph contrastive learning with adaptive augmentation,” in *Proc. Web Conf. (WWW)*, Apr. 2021, pp. 2069–2080.
- [46] B. C. Ross, “Mutual information between discrete and continuous data sets,” *PloS One*, vol. 9, no. 2, p. e87357, Feb. 2014.
- [47] H. B. Creighton and B. McClintock, “A correlation of cytological and genetical crossing-over in Zea mays,” in *Proc. Natl. Acad. Sci.*, 1931, pp. 492–497.
- [48] J. W. Shay and W. E. Wright, “Telomeres and telomerase: Three decades of progress,” *Nat. Rev. Genet.*, vol. 20, no. 5, pp. 299–309, May 2019.
- [49] A. Sanchez, G. Reginato, and P. Cejka, “Crossover or non-crossover outcomes: tailored processing of homologous recombination intermediates,” *Curr. Opin. Genet. Dev.*, vol. 71, pp. 39–47, Dec. 2021.
- [50] D. C. Nageswaran, J. Kim, C. Lambing, J. Kim, J. Park, E.-J. Kim, H. S. Cho, H. Kim, D. Byun, Y. M. Park *et al.*, “HIGH CROSSOVER RATE1 encodes PROTEIN PHOSPHATASE XI and restricts meiotic crossovers in Arabidopsis,” *Nat. Plants*, vol. 7, no. 4, pp. 452–467, Apr. 2021.
- [51] P. Veličković, G. Cucurull, A. Casanova, A. Romero, P. Lio, and Y. Bengio, “Graph attention networks,” in *Proc. Int. Conf. Learn. Represent. (ICLR)*, 2018, pp. 1–12.
- [52] A. F. Agarap, “Deep learning using rectified linear units (ReLU),” *arXiv:1803.08375*, 2018. [Online]. Available: <https://arxiv.org/abs/1803.08375>
- [53] F. Hu, Y. Zhu, S. Wu, L. Wang, and T. Tan, “Hierarchical graph convolutional networks for semi-supervised node classification,” *arXiv:1902.06667*, 2019. [Online]. Available: <https://arxiv.org/abs/1902.06667>
- [54] F. Wang and H. Liu, “Understanding the behaviour of contrastive loss,” in *Proc. IEEE/CVF Conf. Comput. Vis. Pattern Recognit. (CVPR)*, Jun. 2021, pp. 2495–2504.
- [55] J. Ma, W. Tang, J. Zhu, and Q. Mei, “A flexible generative framework for graph-based semi-supervised learning,” in *Proc. Conf. Adv. Neural Inf. Process. Syst. (NeurIPS)*, 2019, pp. 1–10.
- [56] Y. Zhong, X. Wang, Y. Xu, S. Wang, T. Jia, X. Hu, J. Zhao, L. Wei, and L. Zhang, “Mini-UAV-borne hyperspectral remote sensing: From observation and processing to applications,” *IEEE Geosci. Remote Sens. Mag.*, vol. 6, no. 4, pp. 46–62, Dec. 2018.
- [57] Y. Zhong, X. Hu, C. Luo, X. Wang, J. Zhao, and L. Zhang, “WHU-Hi: UAV-borne hyperspectral with high spatial resolution (H2) benchmark datasets and classifier for precise crop identification based on deep convolutional neural network with CRF,” *Remote Sens. Environ.*, vol. 250, p. 112012, Aug. 2020.
- [58] C. Wang, L. Zhang, W. Wei, and Y. Zhang, “Toward effective hyperspectral image classification using dual-level deep spatial manifold representation,” *IEEE Trans. Geosci. Remote Sens.*, early access, Apr. 29, 2021, doi:10.1109/TGRS.2021.3073932.
- [59] P. Sellars, A. I. Aviles-Rivero, and C.-B. Schönlieb, “Superpixel contracted graph-based learning for hyperspectral image classification,” *IEEE Trans. Geosci. Remote Sens.*, vol. 58, no. 6, pp. 4180–4193, Jun. 2020.
- [60] J. Li, X. Huang, P. Gamba, J. M. Bioucas-Dias, L. Zhang, J. A. Benediktsson, and A. Plaza, “Multiple feature learning for hyperspectral image classification,” *IEEE Trans. Geosci. Remote Sens.*, vol. 53, no. 3, pp. 1592–1606, Mar. 2015.
- [61] C. Bo, H. Lu, and D. Wang, “Hyperspectral image classification via JCR and SVM models with decision fusion,” *IEEE Geosci. Remote Sens. Lett.*, vol. 13, no. 2, pp. 177–181, Feb. 2016.
- [62] C. Qin, Y. Wu, J. T. Springenberg, A. Brock, J. Donahue, T. Lillicrap, and P. Kohli, “Training generative adversarial networks by solving ordinary differential equations,” in *Proc. Conf. Adv. Neural Inf. Process. Syst. (NeurIPS)*, 2020, pp. 5599–5609.



Wentao Yu received his B.S. degree from Chengdu University of Information Technology (CUIT), Chengdu, China, in 2018 and his M.S. degree from Xidian University, Xi'an, China, in 2021, respectively. He is currently working toward the Ph.D. degree with the PCA Lab, the Key Laboratory of Intelligent Perception and Systems for High-Dimensional Information of Ministry of Education, the Jiangsu Key Laboratory of Image and Video Understanding for Social Security, and the School of Computer Science and Engineering, Nanjing University of Science and Technology (NJUST), Nanjing, China.

His research interests include deep learning and hyperspectral image processing. His supervisor is Dr. Chen Gong.



Sheng Wan received his B.S. degree from Nanjing Agricultural University (NJAU) in 2016. He is currently working toward the Ph.D. degree with the PCA Lab, the Key Laboratory of Intelligent Perception and Systems for High-Dimensional Information of Ministry of Education, the Jiangsu Key Laboratory of Image and Video Understanding for Social Security, and the School of Computer Science and Engineering, Nanjing University of Science and Technology (NJUST), Nanjing, China.

His research interests include deep learning and hyperspectral image processing. His supervisor is Dr. Chen Gong.



Guangyu Li received the B.S. degree from the China University of Mining and Technology, Xuzhou, China, in 2008, the M.S. degree from Tongji University, Shanghai, China, in 2011, and the Ph.D. degree from the University of Paris-Sud, Paris, France, in 2015.

He is currently an Assistant Professor with the Key Laboratory of Intelligent Perception and Systems for High-Dimensional Information of Ministry of Education, Nanjing University of Science and Technology, Nanjing, China. His research interests include information dissemination in vehicle networks, big data mining, electric vehicles charging/discharging scheduling strategy, and traffic control.



Jian Yang received the Ph.D. degree from Nanjing University of Science and Technology (NJUST), on the subject of pattern recognition and intelligence systems in 2002.

In 2003, he was a Postdoctoral researcher at the University of Zaragoza. From 2004 to 2006, he was a Postdoctoral Fellow at Biometrics Centre of Hong Kong Polytechnic University. From 2006 to 2007, he was a Postdoctoral Fellow at Department of Computer Science of New Jersey Institute of Technology. Now, he is a Chang-Jiang professor in the School of Computer Science and Engineering of NJUST. He is the author of more than 200 scientific papers in pattern recognition and computer vision. His papers have been cited more than 6000 times in the Web of Science, and 17000 times in the Scholar Google. His research interests include pattern recognition, computer vision and machine learning.

Currently, he is/was an associate editor of Pattern Recognition, Pattern Recognition Letters, IEEE Transactions on Neural Networks and Learning Systems, and Neurocomputing. He is a Fellow of IAPR.



Chen Gong received his dual doctoral degree from Shanghai Jiao Tong University (SJTU) and University of Technology Sydney (UTS) in 2016 and 2017, respectively. Currently, he is a full professor in the School of Computer Science and Engineering, Nanjing University of Science and Technology. His research interests mainly include machine learning, data mining, and learning-based vision problems.

He has published more than 100 technical papers at prominent journals and conferences such as JMLR, IEEE T-PAMI, IEEE T-NNLS, IEEE T-IP, IEEE T-CYB, IEEE T-CSVT, IEEE T-MM, IEEE T-ITS, ACM T-IST, ICML, NeurIPS, ICLR, CVPR, AAAI, IJCAI, ICDM, etc. He serves as the associate editor for IEEE T-CSVT and NePL, and also the Area Chair or Senior PC member of several top-tier conferences such as AAAI, IJCAI, ECML, AISTATS, etc.

He won the “Excellent Doctorial Dissertation Award” of Chinese Association for Artificial Intelligence, “Young Elite Scientists Sponsorship Program” of China Association for Science and Technology, “Wu Wen-Jun AI Excellent Youth Scholar Award”, and the Science Fund for Distinguished Young Scholars of Jiangsu Province. He was also selected as the “Global Top Chinese Young Scholars in AI” released by Baidu.

Hyperspectral Image Classification With Contrastive Graph Convolutional Network (Appendix)

Wentao Yu, *Student Member, IEEE*, Sheng Wan, Guangyu Li,
Jian Yang, *Member, IEEE* and Chen Gong, *Senior Member, IEEE*

In this appendix, we first provide some details on four datasets. After that, supplementary experiments are presented, including experiments and ablation study on two additional datasets, the training and inferring time of various methods, and the performance of various methods with a reduced number of training examples.

I. FOUR DATASETS

The details of the four datasets (*i.e.*, *Indian Pines*, *University of Pavia*, *Salinas*, and *Houston University* datasets) are described as follows:

A. Salinas

The *Salinas* dataset was collected by the AVIRIS sensor in Salinas Valley, CA, USA. This dataset comprises 512×217 pixels with a spatial resolution of $3.7 \text{ m} \times 3.7 \text{ m}$. After removing 20 water absorption spectral bands as usual, there are 204 remaining spectral bands. There are 16 land cover categories in this dataset including “Grapes untrained”, “Soil vineyard develop”, “Vineyard vertical trellis”, and so on. The false-color image and ground-truth map of the *Salinas* dataset are exhibited in Fig. 1. The quantities of labeled and unlabeled pixels of various land cover categories used in our experiments are listed in Table I.

B. Indian Pines

The *Indian Pines* dataset was collected in northwestern India, in 1992. This dataset consists of 145×145 pixels with a spatial resolution of $20 \text{ m} \times 20 \text{ m}$. In this dataset, there are 220 spectral bands ranging from 0.4 to $2.5 \mu\text{m}$. As a usual step, 20 water absorption and noisy spectral bands are removed. As a result, 200 spectral bands are remained. There are 16 land cover categories in this dataset, such as “Grass-pasture-mowed”, “Soybean-mintill”, “Buildings-grass-trees-drives”, and so on. The false-color image and ground-truth map of the *Indian Pines* dataset are illustrated in Fig. 2. The quantities of labeled and unlabeled pixels of various land cover categories used in our experiments are listed in Table II.

The authors are with PCA Lab, Key Lab of Intelligent Perception and Systems for High-Dimensional Information of Ministry of Education, and Jiangsu Key Lab of Image and Video Understanding for Social Security, School of Computer Science and Engineering, Nanjing University of Science and Technology, Nanjing, 210094, P.R. China (e-mail: wentao.yu@njust.edu.cn; wan-sheng315@hotmail.com; liuguangyu0627@hotmail.com; csjyang@njust.edu.cn; chen.gong@njust.edu.cn). (*Corresponding authors*: Chen Gong, Guangyu Li.)

TABLE I
QUANTITIES OF LABELED AND UNLABELED PIXELS OF ALL LAND COVER CATEGORIES IN *Salinas* DATASET.

ID	Class	#Labeled	#Unlabeled
1	Broccoli green weeds 1	30	1979
2	Broccoli green weeds 2	30	3696
3	Fallow	30	1946
4	Fallow rough plow	30	1364
5	Fallow smooth	30	2648
6	Stubble	30	3929
7	Celery	30	3549
8	Grapes untrained	30	11241
9	Soil vineyard develop	30	6173
10	Corn senesced green weeds	30	3248
11	Lettuce romaines, 4 wk	30	1038
12	Lettuce romaines, 5 wk	30	1897
13	Lettuce romaines, 6 wk	30	886
14	Lettuce romaines, 7 wk	30	1040
15	Vineyard untrained	30	7238
16	Vineyard vertical trellis	30	1777

TABLE II
QUANTITIES OF LABELED AND UNLABELED PIXELS OF ALL LAND COVER CATEGORIES IN *Indian Pines* DATASET.

ID	Class	#Labeled	#Unlabeled
1	Alfalfa	30	16
2	Corn-notill	30	1398
3	Corn-mintill	30	800
4	Corn	30	207
5	Grass-pasture	30	453
6	Grass-trees	30	700
7	Grass-pasture-mowed	15	13
8	Hay-windrowed	30	448
9	Oats	15	5
10	Soybean-notill	30	942
11	Soybean-mintill	30	2425
12	Soybean-clean	30	563
13	Wheat	30	175
14	Woods	30	1235
15	Buildings-grass-trees-drives	30	356
16	Stone-steel-towers	30	63

C. University of Pavia

In 2001, the *University of Pavia* dataset was captured by the ROSIS sensor in the Pavia University, Italy. This dataset consists of 610×340 pixels with a spatial resolution of $1.3 \text{ m} \times 1.3 \text{ m}$. After removing noisy spectral bands, there are 103 spectral bands in the wavelength ranging from 0.43 to $0.86 \mu\text{m}$. There are 9 land cover categories in this dataset including “Bare soil”, “Painted metal sheets”, “Self-blocking bricks”, and so on. The false-color image and ground-truth map of the *University of Pavia* dataset are illustrated in Fig. 3. The quantities of labeled and unlabeled pixels of various land cover categories used in our experiments are listed in Table III.

TABLE III

QUANTITIES OF LABELED AND UNLABELED PIXELS OF ALL LAND COVER CATEGORIES IN *University of Pavia* DATASET.

ID	Class	#Labeled	#Unlabeled
1	Asphalt	30	6601
2	Meadows	30	18619
3	Gravel	30	2069
4	Trees	30	3034
5	Painted metal sheets	30	1315
6	Bare soil	30	4999
7	Bitumen	30	1300
8	Self-blocking bricks	30	3652
9	Shadows	30	917

TABLE IV

QUANTITIES OF LABELED AND UNLABELED PIXELS OF ALL LAND COVER CATEGORIES IN *Houston University* DATASET.

ID	Class	#Labeled	#Unlabeled
1	Healthy grass	30	1344
2	Stressed grass	30	1424
3	Synthetic grass	30	730
4	Trees	30	1234
5	Soil	30	1268
6	Water	30	295
7	Residential	30	1446
8	Commercial	30	1324
9	Road	30	1524
10	Highway	30	1394
11	Railway	30	1483
12	Parking Lot 1	30	1399
13	Parking Lot 2	30	540
14	Tennis Court	30	451
15	Running Track	30	728

D. Houston University

The *Houston University* dataset covered the Houston University campus and its neighboring areas. In 2013, the *Houston University* dataset was utilized in the Geoscience and Remote Sensing Society Data Fusion Contest. This dataset contains 349×1905 pixels with a spatial resolution of $2.5 \text{ m} \times 2.5 \text{ m}$. In this dataset, there are 156 spectral bands ranging from 380 to 1050 nm. There are 15 land cover categories in this dataset, such as “Tennis Court”, “Road”, “Highway”, and so on. The false-color image and ground-truth map of the *Houston University* dataset are illustrated in Fig. 4. The quantities of labeled and unlabeled pixels of various land cover categories used in our experiments are listed in Table IV.

II. SUPPLEMENTARY EXPERIMENTS

A. Supplementary Datasets

To further evaluate the proposed method, we select *WHU-Hi-HanChuan* and *WHU-Hi-HongHu* datasets [1], [2] to carry out supplementary experiments. They are introduced as follows:

1) *WHU-Hi-HanChuan*: The *WHU-Hi-HanChuan* dataset was collected by a UAV-borne Headwall Nano-Hyperspec sensor in Hanchuan, Hubei province, China. This dataset comprises 1217×303 pixels with a spatial resolution of $0.109 \text{ m} \times 0.109 \text{ m}$. There are 274 spectral bands ranging from 400 to 1000 nm. There are 16 land cover categories in this dataset including “Strawberry”, “Cowpea”, “Soybean”, and so on. The false-color image and ground-truth map of *WHU-Hi-HanChuan* dataset are exhibited in Fig. 5. The quantities of labeled and unlabeled pixels of various land cover categories used in our experiments are listed in Table V.

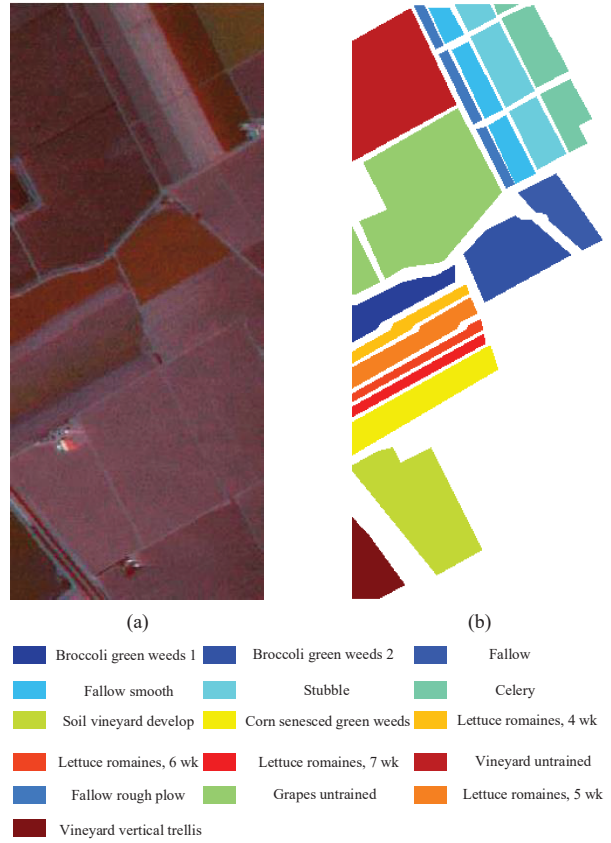


Fig. 1. The *Salinas* dataset. (a) False-color image. (b) Ground-truth map.

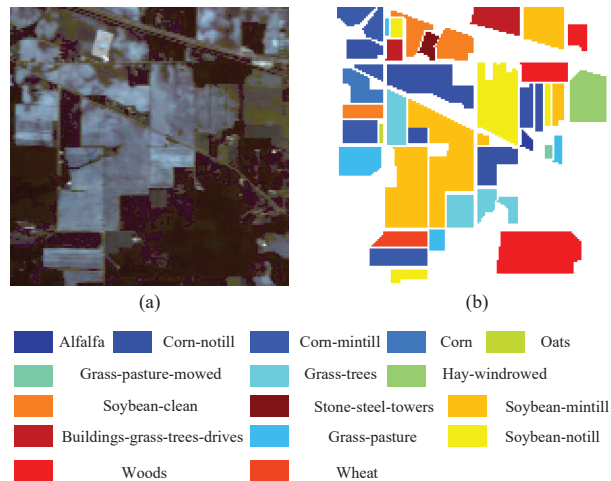


Fig. 2. The *Indian Pines* dataset. (a) False-color image. (b) Ground-truth map.

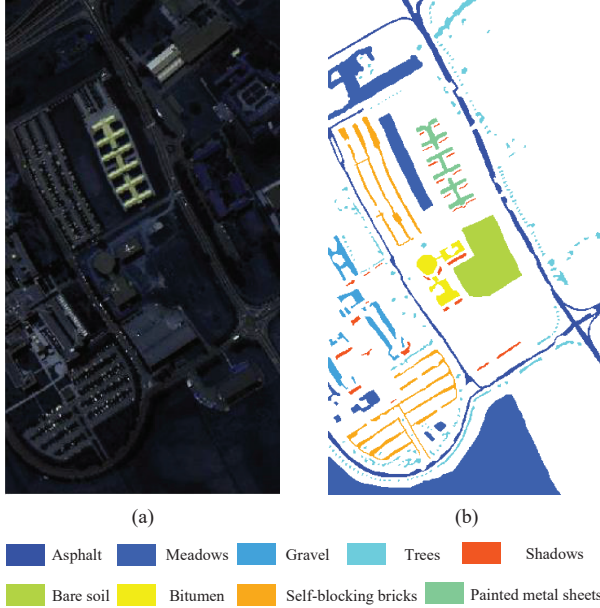


Fig. 3. The *University of Pavia* dataset. (a) False-color image. (b) Ground-truth map.

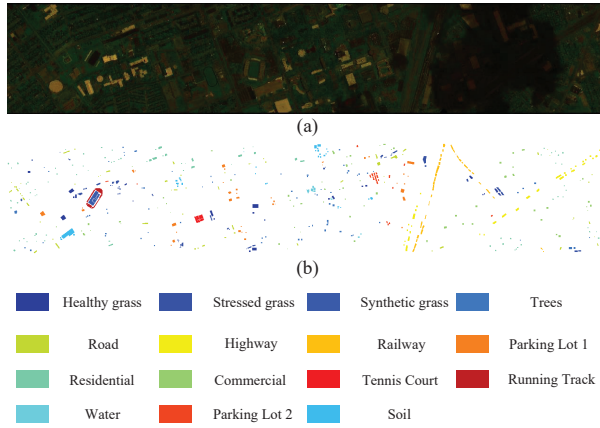


Fig. 4. The *Houston University* dataset. (a) False-color image. (b) Ground-truth map.

2) *WHU-Hi-HongHu*: The *WHU-Hi-HongHu* dataset was collected by a UAV-borne Headwall Nano-Hyperspec sensor in Honghu, Hubei province, China. This dataset comprises 940×475 pixels with a spatial resolution of $0.043 \text{ m} \times 0.043 \text{ m}$. There are 270 spectral bands ranging from 400 to 1000 nm. There are 22 land cover categories in this dataset including “Film covered lettuce”, “Small Brassica chinensis”, “White radish”, and so on. The false-color image and ground-truth map of *WHU-Hi-HongHu* dataset are exhibited in Fig. 6. The quantities of labeled and unlabeled pixels of various land cover categories used in our experiments are listed in Table VI.

B. Experimental Results

Our proposed ConGCN is compared with other baseline methods in both quantitative and qualitative aspects via *WHU-Hi-HanChuan* and *WHU-Hi-HongHu* datasets.

1) *Results on WHU-Hi-HanChuan Dataset*: The quantitative results obtained by different methods on *WHU-Hi-*

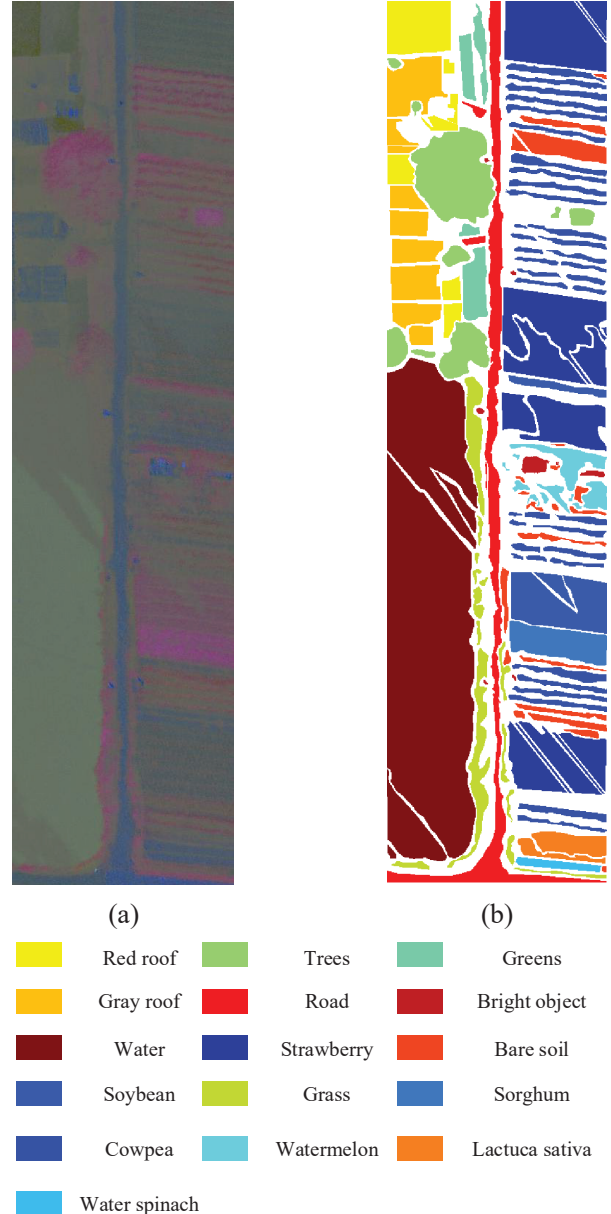


Fig. 5. The *WHU-Hi-HanChuan* dataset. (a) False-color image. (b) Ground-truth map.

HanChuan dataset are summarized in Table VII. We observe that the proposed ConGCN achieves the top-level performance among all the methods in terms of OA, AA, and kappa coefficient. The standard deviations are relatively small as well. Note that the proposed method achieves the highest accuracies on seven land cover categories (*i.e.*, IDs = 1, 2, 6, 8, 9, 11, and 13), and can generally acquire stable and high classification accuracies on the remaining categories. Therefore, it is reasonable to infer that the proposed ConGCN is more stable and effective than the compared methods. Due to the instability of Generative Adversarial Networks (GAN) during training [3], ADGAN has the largest standard deviations. Although SSCL employs contrastive learning, its classification performance is far from perfect, especially in the land cover categories with IDs = 5, 6, 12, 13, and 15. This is

TABLE V

QUANTITIES OF LABELED AND UNLABELED PIXELS OF ALL LAND COVER CATEGORIES IN *WHU-Hi-HanChuan* DATASET.

ID	Class	#Labeled	#Unlabeled
1	Strawberry	30	44705
2	Cowpea	30	22723
3	Soybean	30	10257
4	Sorghum	30	5323
5	Water spinach	30	1170
6	Watermelon	30	4503
7	Greens	30	5873
8	Trees	30	17948
9	Grass	30	9439
10	Red roof	30	10486
11	Gray roof	30	16881
12	Plastic	30	3649
13	Bare soil	30	9086
14	Road	30	18530
15	Bright object	30	1106
16	Water	30	75371

TABLE VI

QUANTITIES OF LABELED AND UNLABELED PIXELS OF ALL LAND COVER CATEGORIES IN *WHU-Hi-HongHu* DATASET.

ID	Class	#Labeled	#Unlabeled
1	Red roof	30	14011
2	Road	30	3482
3	Bare soil	30	21791
4	Cotton	30	163255
5	Cotton firewood	30	6188
6	Rape	30	44527
7	Chinese cabbage	30	24073
8	Pakchoi	30	4024
9	Cabbage	30	10789
10	Tuber mustard	30	12364
11	Brassica parachinensis	30	10985
12	Brassica chinensis	30	8924
13	Small Brassica chinensis	30	22477
14	Lactuca sativa	30	7326
15	Celtuce	30	972
16	Film covered lettuce	30	7232
17	Romaine lettuce	30	2980
18	Carrot	30	3187
19	White radish	30	8682
20	Garlic sprout	30	3456
21	Broad bean	30	1298
22	Tree	30	4010

because SSCL only utilizes unlabeled examples to pre-train the encoder and simply fine-tunes the network with very few labeled examples. Different from SSCL, our proposed ConGCN utilizes the unlabeled data and the available class information, simultaneously, via using a semi-supervised contrastive loss. As a result, our proposed method outperforms the baseline methods. In addition, it can be observed that the performance gap between the four traditional HSI classification methods is enormous. For example, the OA of PKCRC is lower than 70% while the OA of JSDF is higher than 90%. To be specific, PKCRC is a kernel-based approach, which obtains a set of classification probability maps using spectral information. Different from PKCRC, JSDF is based on the joint collaborative representation and support vector machine with decision fusion, thus revealing better representation ability than PKCRC.

Fig. 7 shows a visual comparison of the classification maps generated by different methods on *WHU-Hi-HanChuan* dataset, where the ground-truth map is exhibited in Fig. 7(b). The classification maps obtained by SMR (Fig. 7(c)), SSCL (Fig. 7(f)), and MFL (Fig. 7(j)) suffer from pepper-noise-

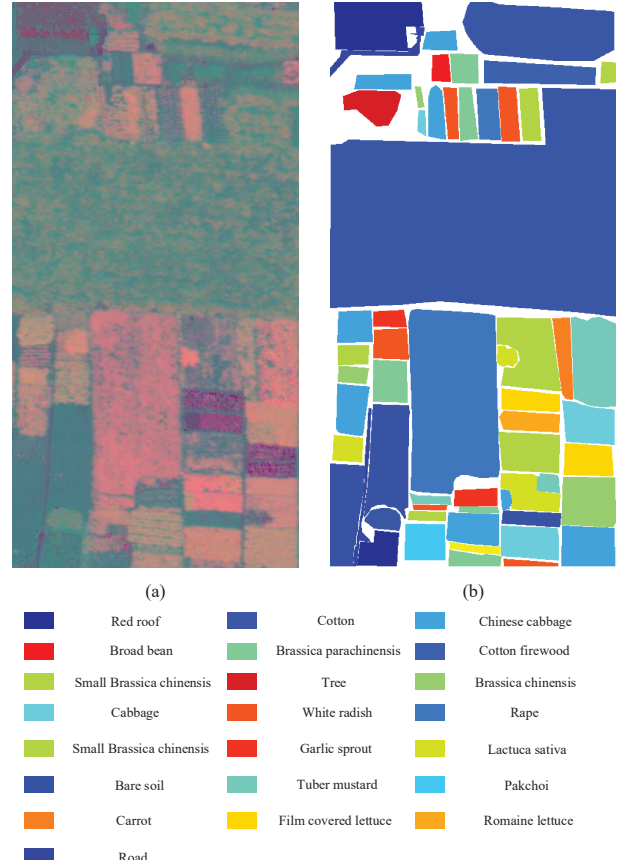


Fig. 6. The *WHU-Hi-HongHu* dataset. (a) False-color image. (b) Ground-truth map.

like mistakes within multiple areas. For instance, the middle parts of the classification maps obtained by SMR (Fig. 7(c)), SSCL (Fig. 7(f)), and MFL (Fig. 7(j)) are highly confusing. Comparatively, the classification map of the proposed ConGCN method yields a smoother visual effect and shows fewer misclassifications than the compared methods.

2) *Results on WHU-Hi-HongHu Dataset:* Table VIII presents the quantitative results of different methods on *WHU-Hi-HongHu* dataset. Similar to the results on *WHU-Hi-HanChuan* dataset, the results in Table VIII indicate that the proposed ConGCN outperforms the compared methods in terms of OA, AA, and kappa coefficient, which again validates the strength of our proposed contrastive learning-based graph convolution. Moreover, compared with the CNN-based methods (*i.e.*, A²S²K and ASSMN), the proposed ConGCN increases the OAs by 11.85% and 18.90%, respectively, which suggests that the spatial relations captured by our ConGCN are more useful than the information characterized by fixed convolutional kernels of CNN. Meanwhile, we can observe that the OA of IFRF is lower than that of ConGCN. We speculate that the supervision signals extracted from the spectral-spatial information of HSI are more dominant in improving the model performance, compared with the recursive filtering employed by IFRF. Therefore, our proposed ConGCN achieves stable and encouraging performance.

Fig. 8 visualizes the classification results generated by

TABLE VII
PER-CLASS ACCURACY, OAS, AAS (%), AND KAPPA COEFFICIENTS ACHIEVED BY DIFFERENT METHODS ON *WHU-Hi-HanChuan* DATASET. THE BEST AND SECOND BEST RECORDS IN EACH ROW ARE **BOLDED** AND UNDERLINED, RESPECTIVELY.

ID	SMR [4]	MSSGU [5]	SGL [6]	SSCL [7]	A ² S ² K [8]	ASSMN [9]	ADGAN [10]	MFL [11]	JSDF [12]	PKCRC [13]	IFRF [14]	ConGCN
1	70.91±7.50	98.35±0.53	79.11±5.86	90.32±2.72	93.39±0.73	79.11±3.78	14.11±19.57	79.55±4.88	91.02±1.85	71.32±1.70	91.45±3.68	99.74±0.42
2	49.70±21.48	96.46±1.15	69.68±3.34	59.32±9.93	96.93±1.18	90.18±4.02	88.39±6.20	63.92±4.13	80.27±3.91	44.00±11.05	82.46±5.18	97.04±2.69
3	75.36±8.30	98.62±0.43	87.47±7.47	36.26±12.05	<u>77.53±1.47</u>	84.85±2.37	46.25±21.84	70.80±5.37	89.05±0.72	77.18±7.67	76.82±4.57	98.58±2.47
4	93.30±4.36	98.96±0.24	95.84±1.71	75.17±9.26	85.05±0.17	93.90±1.71	72.76±19.97	92.95±3.16	95.86±0.33	98.34±0.90	86.40±5.84	98.42±3.37
5	73.99±6.59	100.00±0.00	98.68±1.38	1.53±3.20	41.50±2.66	98.21±0.98	99.31±0.91	91.26±2.60	<u>99.32±0.00</u>	91.17±8.89	80.95±5.94	98.93±0.64
6	42.58±12.72	97.45±0.75	75.68±7.48	1.39±1.71	65.47±6.36	61.90±4.53	55.79±16.46	64.00±4.63	80.12±4.53	51.72±10.40	63.62±7.86	98.08±3.23
7	87.47±2.80	99.99±0.01	97.49±0.73	62.39±20.53	51.70±5.81	89.07±4.18	97.35±2.83	95.09±1.93	97.51±1.12	4.69±13.90	58.29±6.41	99.28±0.33
8	37.45±11.08	93.57±2.09	80.03±6.78	39.41±7.81	94.39±1.21	67.13±5.96	75.96±11.10	58.61±4.32	81.32±3.03	44.33±8.48	84.85±5.08	98.02±1.30
9	47.23±12.67	93.10±0.87	82.30±8.10	11.66±7.51	73.27±1.25	75.51±8.08	55.64±11.72	50.50±3.49	88.14±0.26	39.18±9.98	57.00±5.11	95.01±1.14
10	81.28±10.02	93.50±0.73	83.65±4.41	29.11±5.77	94.85±2.55	77.58±4.30	44.17±17.75	81.38±5.15	96.46±0.33	34.52±3.75	78.91±4.78	95.89±1.65
11	76.60±11.18	91.26±0.64	95.83±1.25	44.82±13.68	78.31±4.37	81.69±8.60	63.80±26.60	83.71±4.74	95.76±1.40	61.27±8.07	89.07±5.45	99.13±0.56
12	48.22±13.53	99.98±0.03	92.81±0.38	3.04±5.04	59.87±0.82	94.60±2.34	75.15±21.83	88.40±2.97	91.63±1.80	75.90±29.83	86.55±3.61	99.64±0.10
13	39.86±8.01	77.36±2.61	60.21±6.21	8.74±6.10	67.46±4.46	64.63±5.16	51.29±5.12	59.99±7.81	76.80±4.07	74.94±6.20	66.30±3.90	91.44±1.32
14	57.06±10.59	91.94±0.87	68.11±9.41	70.18±7.27	82.66±4.83	81.07±7.23	52.13±10.89	81.13±4.56	80.39±0.32	33.36±8.97	77.01±5.08	90.56±1.94
15	78.82±18.30	95.11±1.26	79.55±11.29	0.00±0.00	74.34±3.87	94.34±1.66	89.78±7.65	78.92±4.93	96.61±1.13	80.83±5.67	51.47±15.13	91.78±0.03
16	96.30±1.00	99.21±0.14	77.84±5.64	98.70±0.89	97.38±0.16	97.15±1.83	75.23±24.70	84.63±4.80	98.24±0.57	100.00±0.00	99.61±0.27	99.09±0.38
OA	72.08±4.31	96.10±0.28	79.23±2.03	67.02±2.10	86.63±0.46	84.98±1.11	59.69±11.12	77.09±1.94	90.72±0.15	68.60±0.84	84.85±1.49	97.71±0.58
AA	66.01±5.47	95.30±0.31	82.77±0.89	39.50±2.78	77.13±0.61	83.18±2.04	66.07±7.08	76.55±1.09	89.91±0.15	61.42±1.65	76.92±1.63	96.92±0.58
kappa	67.76±4.93	95.44±0.33	76.31±2.23	60.73±2.58	84.43±0.52	82.52±2.42	51.86±12.79	73.66±2.10	89.19±0.18	62.42±1.02	82.43±1.68	97.32±0.68

different methods on *WHU-Hi-HongHu* dataset. As depicted in Fig. 8(n), the classification map of our proposed ConGCN is noticeably closer to the ground-truth map (Fig. 8(b)) than those of other methods, which is consistent with the previous results in Table VIII. Besides, A²S²K (Fig. 8(g)) and ASSMN (Fig. 8(h)), which use fixed convolutional kernels, produce more errors than ConGCN. In the classification map of ADGAN (Fig. 8(i)), most of the pixels are misclassified, which explains the cause of ADGAN’s poor performance in terms of OA. It is also notable that large numbers of pixels in the classification map of SSCL (Fig. 8(f)) are misclassified. This indicates that the performance of simply using the traditional paradigm of contrastive learning is far from satisfactory, especially with very few labeled examples.

C. Ablation Study

To further shed light on the contributions of the proposed components (*i.e.*, the semi-supervised contrastive loss, the graph generative loss, the spatial-level graph augmentation, and the spectral-level graph augmentation), we select *WHU-Hi-HanChuan* and *WHU-Hi-HongHu* datasets to carry out supplementary ablation experiments. The number of labeled pixels per class is kept identical to the experimental settings in Section VII-A of the main paper. Every time we report the OA, AA, and kappa coefficient obtained by ConGCN without one of the aforementioned components. For simplicity, “w/o CLoss” and “w/o GLoss” indicate the reduced models by removing the contrastive loss function \mathcal{L}_{ssc} and the graph generative loss \mathcal{L}_{g^2} , respectively. In addition, we utilize “w/o SpaAug” and “w/o SpeAug” to indicate the reduced models that remove the spatial-level graph augmentation and the spectral-level graph augmentation, respectively. Moreover, “w/o CGSS” is used to indicate the reduced model that removes the semi-supervised contrastive loss, graph generative loss, spatial-level graph augmentation, and spectral-level graph augmentation, simultaneously. Concretely, Table IX and Table X exhibit the corresponding results, respectively. It can be found that the OA of each reduced model is lower than ConGCN. Besides, the OA of “w/o CGSS” is the lowest among all reduced models on each dataset. It proves that the good performance of our proposed ConGCN can be attributable to each component. We can also observe that the reduced model

“w/o GLoss” consistently achieves higher OAs, AAs, and kappa coefficients than “w/o CLoss” on *WHU-Hi-HanChuan* and *WHU-Hi-HongHu* datasets, which validates that the semi-supervised contrastive loss makes a greater contribution than the generative loss to performance improvement.

D. Comparison of Training and Inferring Time

To reveal the advantage of our proposed ConGCN over the baseline methods in terms of efficiency, Table XI and Table XII report the training and inferring time of different methods on six datasets (*i.e.*, *Indian Pines*, *University of Pavia*, *Salinas*, *Houston University*, *WHU-Hi-HanChuan*, and *WHU-Hi-HongHu* datasets), respectively, where the number of labeled pixels per class is kept identical to the experimental settings in Section VII-A of the main paper. The codes for all the methods are written in Python (except MFL [11], JSDF [12], PKCRC [13], and IFRF [14]). The experiments are conducted on a server with a 2.20-GHz Intel Xeon E5-2650 v4 CPU with 64 GB of RAM and an NVIDIA GeForce RTX 2080Ti GPU with 11GB of memory. Since MSSGU [5] is not scalable to large datasets such as *Houston University*, *WHU-Hi-HanChuan*, and *WHU-Hi-HongHu* datasets, and SGL [6] is also not applicable to *WHU-Hi-HongHu* dataset, we do not report the corresponding training and inferring time of MSSGU and SGL here. MFL, JSDF, PKCRC, and IFRF are conducted with MATLAB R2021b on a CPU. Among traditional HSI classification methods, PKCRC and IFRF take the least and the second least training time among all the methods on six datasets, respectively. In Table XI, we can see that ConGCN takes the least training time among all the deep learning-based methods (*i.e.*, all the methods except MFL, JSDF, PKCRC, and IFRF) on *Indian Pines*, *University of Pavia*, *Houston University*, *WHU-Hi-HanChuan*, and *WHU-Hi-HongHu* datasets. Since performing localized and hierarchical graph convolution simultaneously is time-consuming on the large-scale dataset (*i.e.*, *Salinas* dataset), our proposed ConGCN cannot be as efficient as MSSGU, ASSMN, and ADGAN. In Table XII, we can observe that ConGCN takes the least inferring time among all the methods on six datasets, which demonstrates that our proposed method is efficient for HSI classification in the phase of label inference.

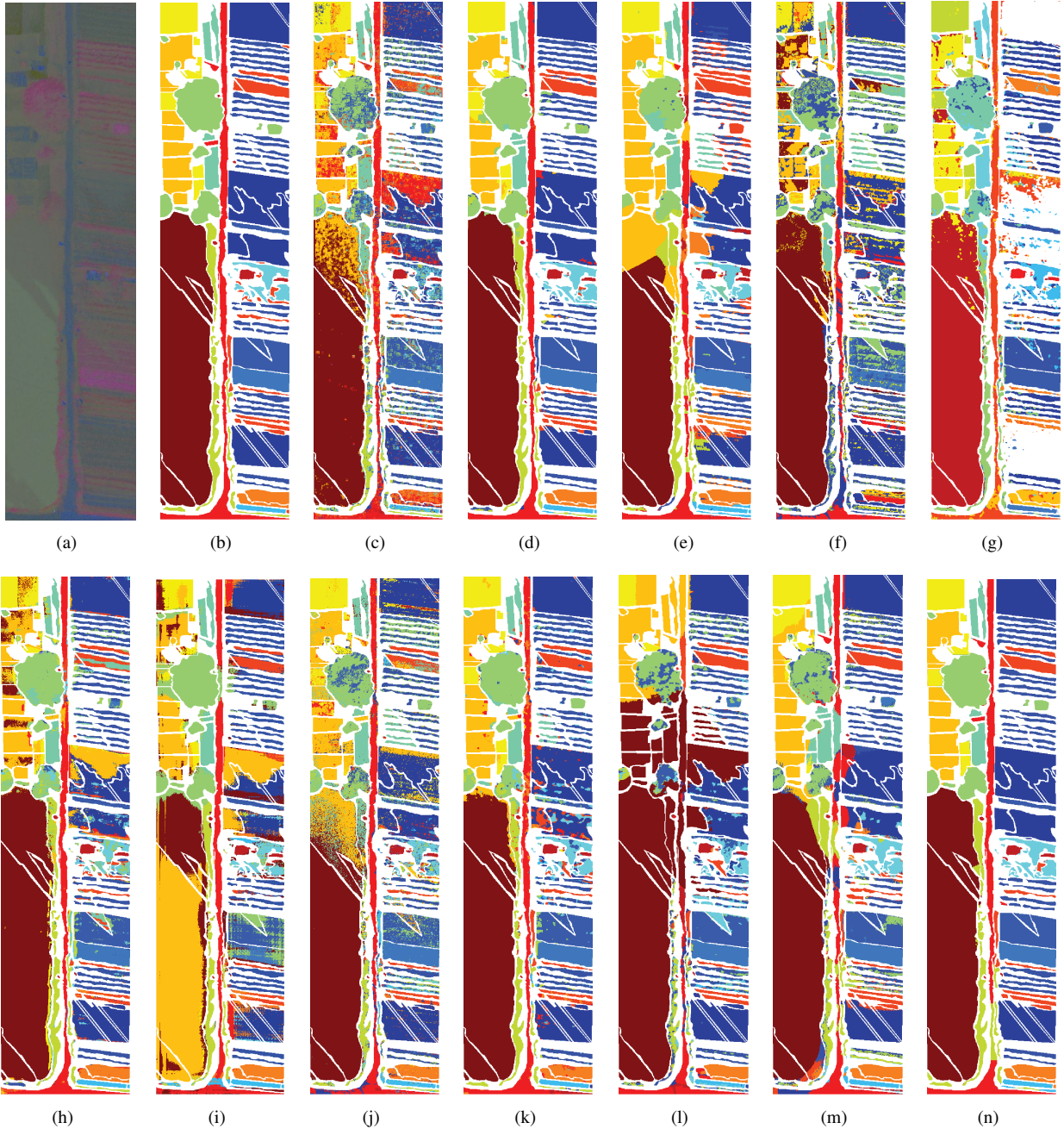


Fig. 7. Classification maps obtained by different methods on *WHU-Hi-HanChuan* dataset. (a) False-color image. (b) Ground-truth map. (c) SMR. (d) MSSGU. (e) SGL. (f) SSCL. (g) A^2S^2K . (h) ASSMN. (i) ADGAN. (j) MFL. (k) JSDF. (l) PKCRC. (m) IFRF. (n) ConGCN (Proposed).

E. Impact of the Number of Labeled Examples

In this subsection, AAs and kappa coefficients of the proposed ConGCN and baseline methods under different numbers of labeled examples are shown in Fig. 9 and Fig. 10, respectively. We vary the number of labeled examples per class from 5 to 30 with an interval of 5 and report the AAs and kappa coefficients gained by all the methods on six datasets (*i.e.*, *Indian Pines*, *University of Pavia*, *Salinas*, *Houston University*, *WHU-Hi-HanChuan*, and *WHU-Hi-HongHu* datasets). As observed in Fig. 9 and Fig. 10, the AAs and kappa coefficients of ADGAN could drop significantly on the *Indian Pines* (Fig. 9(a) and Fig. 10(a)), *University of Pavia*

(Fig. 9(b) and Fig. 10(b)), *Salinas* (Fig. 9(c) and Fig. 10(c)), and *Houston University* (Fig. 9(d) and Fig. 10(d)) datasets even when the number of labeled examples increases. It is consistent with the corresponding OAs of ADGAN under different numbers of labeled examples, which are presented in the paper. Thanks to the exploration of the supervision signals from both spectral and spatial aspects of HSI, our proposed ConGCN still achieves relatively high AAs and kappa coefficients even if the labeled examples are quite limited (*i.e.*, five or ten labeled examples per class), which suggests the good stability of ConGCN in HSI classification.

TABLE VIII

PER-CLASS ACCURACY, OAs, AAs (%), AND KAPPA COEFFICIENTS ACHIEVED BY DIFFERENT METHODS ON *WHU-Hi-HongHu* DATASET. THE BEST AND SECOND BEST RECORDS IN EACH ROW ARE **BOLDED** AND UNDERLINED, RESPECTIVELY.

ID	SMR [4]	MSSGU [5]	SGL [6]	SSCL [7]	A^2S^2K [8]	ASSMN [9]	ADGAN [10]	MFL [11]	JSDF [12]	PKCRC [13]	IFRF [14]	ConGCN
1	79.98±5.95	92.58±1.10	82.44±3.10	71.19±11.69	97.79±0.46	90.16±1.97	89.53±5.85	76.24±3.86	95.40±0.41	92.97±4.73	96.54±1.70	93.49±0.55
2	86.96±7.40	97.71±0.35	78.29±5.44	15.13±18.72	59.92±2.66	92.24±3.78	63.68±16.57	87.87±2.03	95.26±0.98	87.15±7.17	61.23±7.35	88.87±0.03
3	77.76±7.74	95.97±0.54	86.92±2.13	86.94±6.01	95.08±0.41	80.64±1.86	47.88±20.18	84.11±2.42	87.43±1.53	83.44±1.84	97.46±1.40	98.44±0.01
4	78.05±0.34	97.07±1.53	90.16±5.89	97.49±1.60	<u>99.58±0.03</u>	81.27±3.66	35.06±21.67	83.30±3.24	88.13±4.68	87.37±3.06	99.73±0.12	97.84±1.34
5	71.88±7.65	<u>98.77±0.45</u>	97.10±2.25	3.44±5.77	35.05±2.94	<u>82.15±5.04</u>	83.03±19.67	78.98±2.84	92.20±1.88	89.22±2.08	73.49±4.73	100.00±0.00
6	81.91±11.89	97.19±0.58	91.85±1.77	87.18±2.49	91.59±0.57	89.90±1.19	22.25±24.19	81.97±2.78	96.07±2.09	87.80±2.03	97.44±1.57	99.91±0.19
7	56.55±10.74	91.81±1.89	69.70±5.74	59.89±8.93	83.03±1.20	64.05±3.79	15.50±11.33	55.02±3.05	78.76±2.50	60.96±4.11	88.40±2.09	94.01±0.75
8	40.03±6.15	98.37±0.93	91.75±11.13	0.43±0.64	56.36±4.37	52.40±7.48	15.78±15.50	65.97±4.39	89.82±1.73	44.39±2.40	46.65±7.46	99.63±0.00
9	84.83±17.61	99.28±0.32	93.59±3.37	85.49±4.73	98.69±0.19	93.22±1.64	44.92±20.67	93.44±1.50	97.08±2.08	90.50±2.14	96.21±3.24	99.33±0.08
10	57.10±16.66	82.04±1.56	80.96±3.99	35.02±8.79	80.96±5.42	62.08±6.14	98.68±0.81	70.82±3.95	77.05±8.99	65.84±3.63	89.04±3.21	97.38±1.30
11	43.32±13.31	95.26±0.88	83.40±5.10	11.01±12.62	77.14±4.37	50.33±6.93	17.85±16.15	55.95±5.61	86.04±2.74	52.63±5.97	76.18±3.94	94.67±0.49
12	51.60±26.14	94.33±0.52	83.37±5.69	45.60±4.16	53.49±1.51	68.61±6.83	52.97±19.11	75.27±3.86	78.83±1.33	66.53±3.95	63.11±6.32	95.50±0.60
13	59.18±12.27	89.94±0.79	75.41±7.32	57.37±10.31	73.89±4.18	57.60±8.10	40.34±17.09	56.78±6.05	79.77±0.95	64.96±2.71	84.25±4.17	93.05±1.63
14	87.01±8.80	97.66±0.35	85.03±2.10	6.24±7.32	75.85±4.64	78.63±4.94	84.10±9.91	61.33±4.34	91.18±0.91	71.73±5.71	90.71±6.35	98.03±0.10
15	78.11±13.51	99.89±0.14	97.11±0.38	0.00±0.00	62.06±3.45	96.30±1.61	71.67±24.10	95.82±3.07	99.49±0.00	97.14±1.68	59.63±11.93	98.29±0.23
16	90.59±8.85	97.25±0.40	86.11±4.67	78.41±12.99	93.43±1.30	90.99±3.91	98.18±3.24	79.31±3.15	93.34±1.28	91.38±2.64	98.80±0.57	97.88±0.32
17	75.82±10.06	99.85±0.17	87.43±8.18	13.31±22.51	88.93±4.86	78.54±7.02	75.72±9.40	95.38±1.77	98.12±0.34	89.13±3.76	84.78±6.08	92.42±7.87
18	78.81±16.42	97.56±1.22	92.41±3.24	5.56±8.68	76.46±0.57	82.97±5.52	82.75±17.29	80.77±4.80	79.77±0.27	93.58±1.84	62.60±6.07	98.06±0.26
19	70.25±11.41	93.14±0.54	74.58±5.24	31.81±17.45	87.89±2.74	72.15±3.39	4.43±5.02	74.99±4.55	92.04±0.31	81.82±7.02	82.01±4.89	98.37±1.13
20	70.69±15.40	98.35±0.68	97.46±1.50	3.14±5.70	67.58±8.03	80.40±7.82	4.19±5.69	88.82±2.31	95.99±0.88	95.60±1.36	56.42±6.13	99.89±0.04
21	67.66±31.40	100.00±0.00	99.85±0.00	0.00±0.00	47.32±10.41	69.95±12.42	62.80±28.39	93.16±2.35	99.88±0.12	96.32±4.52	67.06±8.42	99.85±0.00
22	90.48±9.17	98.60±0.77	99.08±0.47	13.31±17.47	34.28±5.59	85.74±4.92	96.34±6.02	86.18±4.34	94.86±0.35	91.08±4.04	60.95±12.27	99.98±0.02
OA	73.87±5.31	95.62±0.60	86.91±2.30	73.48±1.10	85.47±0.15	78.42±3.31	41.11±10.08	77.88±1.57	88.58±2.43	81.84±1.25	90.49±0.55	97.32±0.63
AA	71.76±5.14	96.03±0.17	87.45±0.99	36.73±1.92	74.38±0.13	77.29±4.11	54.89±8.86	78.25±0.92	91.12±0.52	80.98±0.64	78.76±0.92	97.04±0.39
kappa	68.71±5.79	94.50±0.74	83.85±2.63	65.74±1.47	82.12±0.18	73.86±3.81	36.00±8.57	73.05±1.74	85.95±2.85	77.69±1.39	88.07±0.67	96.63±0.78

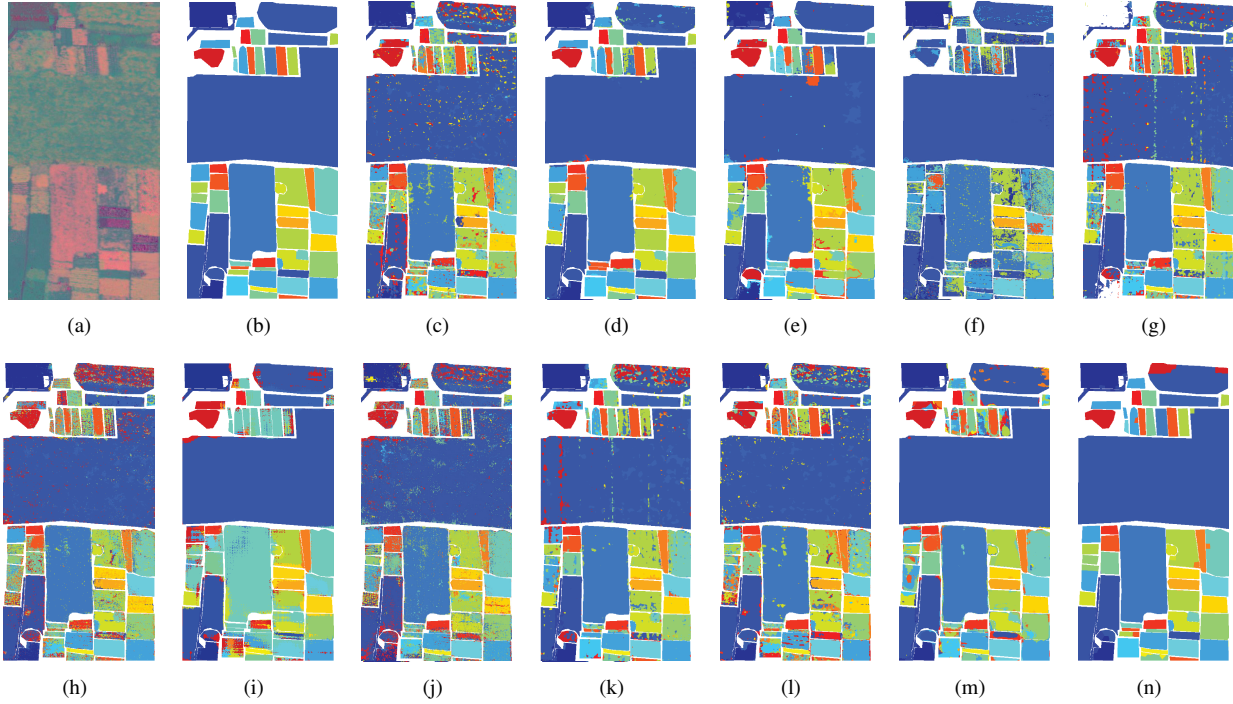


Fig. 8. Classification maps obtained by different methods on *WHU-Hi-HongHu* dataset. (a) False-color image. (b) Ground-truth map. (c) SMR. (d) MSSGU. (e) SGL. (f) SSCL. (g) A^2S^2K . (h) ASSMN. (i) ADGAN. (j) MFL. (k) JSDF. (l) PKCRC. (m) IFRF. (n) ConGCN (Proposed).

TABLE IX

OAs, AAs (%), AND KAPPA COEFFICIENTS ACHIEVED BY DIFFERENT SETTINGS ON *WHU-Hi-HanChuan* DATASET. THE BEST AND SECOND BEST RECORDS IN EACH ROW ARE **BOLDED** AND UNDERLINED, RESPECTIVELY.

metrics	w/o CLoss	w/o GLoss	w/o SpaAug	w/o SpeAug	w/o CGSS	ConGCN
OA	96.70±1.09	96.87±0.68	97.40±0.25	97.17±0.41	95.62±0.47	97.71±0.58
AA	96.02±0.86	96.15±0.66	96.76±0.25	96.39±0.42	94.66±0.79	96.92±0.58
kappa	96.15±1.27	96.34±0.80	96.96±0.29	96.69±0.48	94.88±0.56	97.32±0.68

F. Reducing the Number of Training Examples

To verify the effectiveness of the proposed ConGCN when given limited labeled examples, we only use 1, 2, 3, and 4 labeled examples per class for training and report the OAs,

TABLE X

OAs, AAs (%), AND KAPPA COEFFICIENTS ACHIEVED BY DIFFERENT SETTINGS ON *WHU-Hi-HanChuan* DATASET. THE BEST AND SECOND BEST RECORDS IN EACH ROW ARE **BOLDED** AND UNDERLINED, RESPECTIVELY.

metrics	w/o CLoss	w/o GLoss	w/o SpaAug	w/o SpeAug	w/o CGSS	ConGCN
OA	96.25±3.32	96.51±0.88	97.00±0.66	96.79±0.88	95.77±0.91	97.32±0.63
AA	96.44±1.83	96.77±0.47	96.75±0.53	96.82±0.39	96.37±0.37	97.04±0.39
kappa	95.33±4.04	95.63±1.08	96.23±0.82	95.97±1.09	94.71±1.11	96.63±0.78

AAs, and kappa coefficients gained by all the methods on six datasets (*i.e.*, Indian Pines, University of Pavia, Salinas, Houston University, *WHU-Hi-HanChuan*, and *WHU-Hi-HongHu* datasets), respectively. Fig. 11, Fig. 12, and Fig. 13

TABLE XI
TRAINING TIME (IN SECONDS) OF DIFFERENT METHODS ON SIX DATASETS. THE BEST RECORDS IN EACH ROW ARE **BOLDED**.

Dataset	SMR [4]	MSSGU [5]	SGL [6]	SSCL [7]	A ² S ² K [8]	ASSMN [9]	ADGAN [10]	MFL [11]	JSDF [12]	PKCRC [13]	IFRF [14]	ConGCN
<i>Indian Pines</i>	3381.67	243.63	340.45	1607.37	306.68	361.43	348.59	7.53	26.03	0.15	4.70	192.04
<i>University of Pavia</i>	3467.27	235.86	221.08	1370.77	258.09	275.87	221.00	13.06	33.82	0.80	6.62	181.01
<i>Salinas</i>	6814.97	292.81	729.24	2421.64	586.21	346.98	372.86	16.30	87.10	0.85	6.55	488.40
<i>Houston University</i>	3806.39	-	631.96	1452.77	419.24	321.77	355.01	54.63	73.68	4.50	29.43	304.06
<i>WHU-Hi-HanChuan</i>	10450.34	-	429.08	3158.93	360.66	516.40	435.34	50.94	37.68	3.22	19.20	289.34
<i>WHU-Hi-HongHu</i>	15080.02	-	-	4408.46	405.47	534.64	599.81	72.72	47.93	5.01	28.91	291.70

TABLE XII
INFERRING TIME (IN SECONDS) OF DIFFERENT METHODS ON SIX DATASETS. THE BEST RECORDS IN EACH ROW ARE **BOLDED**.

Dataset	SMR [4]	MSSGU [5]	SGL [6]	SSCL [7]	A ² S ² K [8]	ASSMN [9]	ADGAN [10]	MFL [11]	JSDF [12]	PKCRC [13]	IFRF [14]	ConGCN
<i>Indian Pines</i>	1.69	0.41	2.63	1.61	1.53	1.81	0.70	0.17	24.90	0.07	0.08	0.05
<i>University of Pavia</i>	1.73	0.40	1.70	1.37	1.29	1.38	0.44	0.31	32.49	0.67	0.12	0.05
<i>Salinas</i>	3.41	0.49	5.63	2.42	2.93	1.73	0.75	0.35	85.52	0.38	0.12	0.12
<i>Houston University</i>	1.90	-	4.88	1.45	2.10	1.61	0.71	1.12	68.52	2.48	0.53	0.08
<i>WHU-Hi-HanChuan</i>	5.23	-	3.30	3.16	1.36	2.58	0.87	1.03	35.35	1.58	0.34	0.07
<i>WHU-Hi-HongHu</i>	7.54	-	-	4.41	2.03	2.67	1.20	1.43	45.54	1.98	0.52	0.07

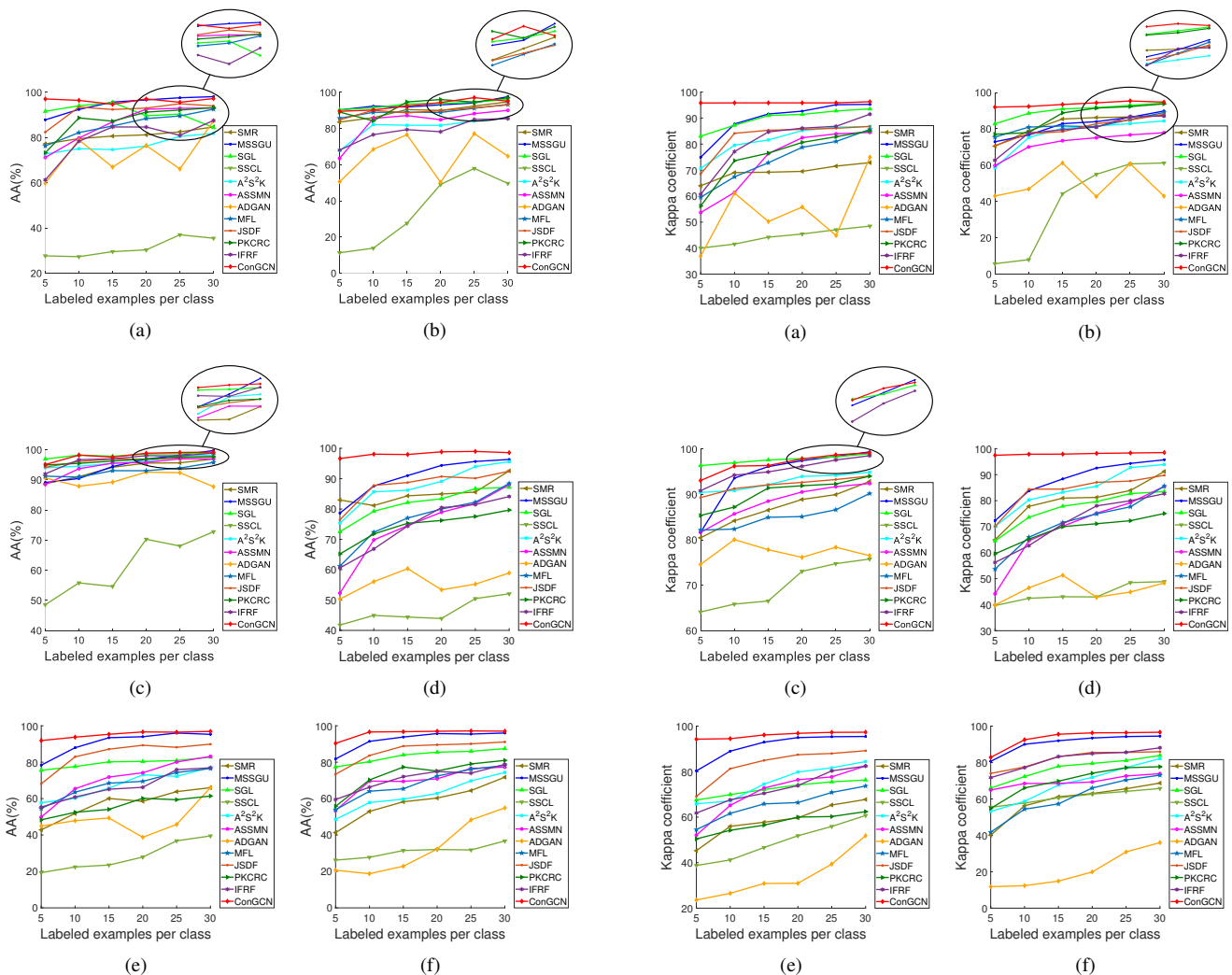
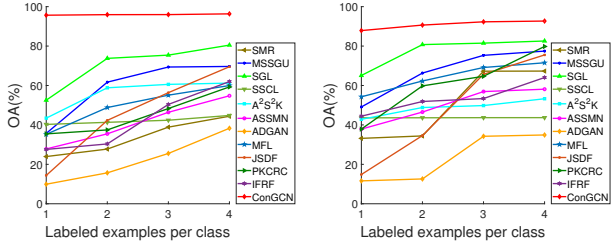
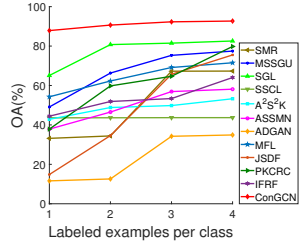


Fig. 9. AAs of various methods under different numbers of labeled examples per class. (a) *Indian Pines* dataset. (b) *University of Pavia* dataset. (c) *Salinas* dataset. (d) *Houston University* dataset. (e) *WHU-Hi-HanChuan* dataset. (f) *WHU-Hi-HongHu* dataset.

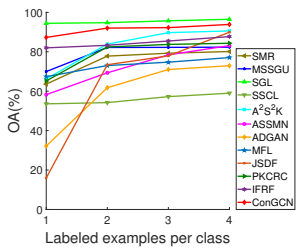
Fig. 10. Kappa coefficients of various methods under different numbers of labeled examples per class. (a) *Indian Pines* dataset. (b) *University of Pavia* dataset. (c) *Salinas* dataset. (d) *Houston University* dataset. (e) *WHU-Hi-HanChuan* dataset. (f) *WHU-Hi-HongHu* dataset.



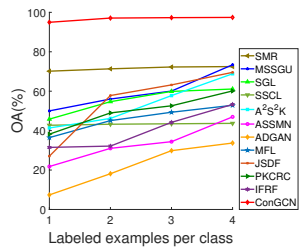
(a)



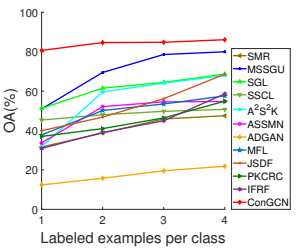
(b)



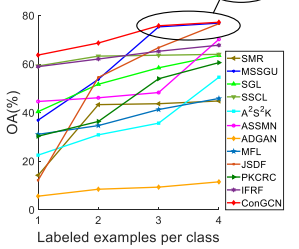
(c)



(d)



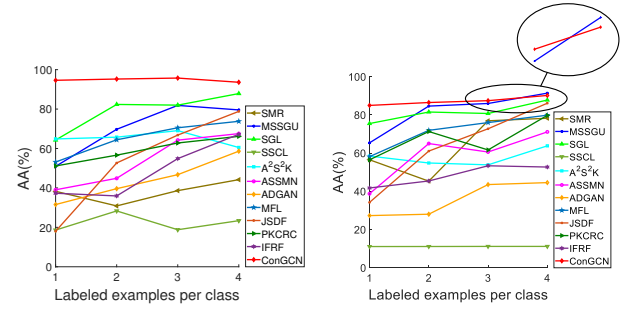
(e)



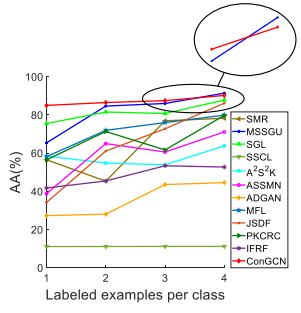
(f)

Fig. 11. OAs of various methods under different numbers of labeled examples per class (*i.e.*, 1, 2, 3, and 4 labeled examples per class). (a) *Indian Pines* dataset. (b) *University of Pavia* dataset. (c) *Salinas* dataset. (d) *Houston University* dataset. (e) *WHU-Hi-HanChuan* dataset. (f) *WHU-Hi-HongHu* dataset.

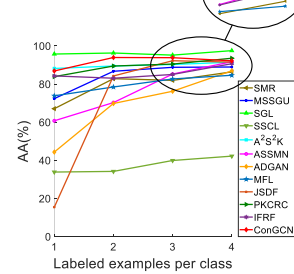
show the OAs, AAs, and kappa coefficients under different numbers of labeled examples, respectively. As observed in Fig. 11, the OAs of all the methods degrade by decreasing the number of labeled examples. Thanks to the supervision signals explored from the spectral-spatial information of HSI, our proposed ConGCN still achieves relatively high OAs even if the labeled examples are extremely limited on six datasets (*i.e.*, one or two labeled examples per class), which suggests the good stability of ConGCN in HSI classification. In Fig. 12 and Fig. 13, the AAs and kappa coefficients of several baseline methods are not stable. For example, the AAs of MSSGU could drop on the *Indian Pines* (Fig. 12(a)) and *WHU-Hi-HongHu* (Fig. 12(f)) datasets when the number of labeled examples increases. Besides, the kappa coefficients of SMR could drop on the *University of Pavia* (Fig. 13(b)) and *WHU-Hi-HongHu* (Fig. 13(f)) datasets when the number of labeled examples increases. This indicates that the stability of MSSGU and SMR is relatively poor when given limited labeled examples.



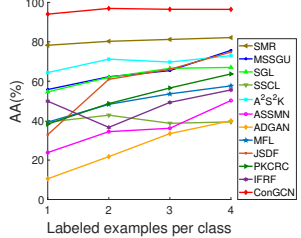
(a)



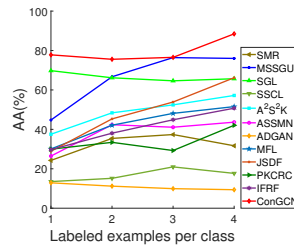
(b)



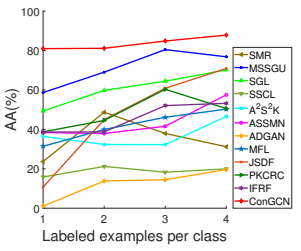
(c)



(d)



(e)



(f)

Fig. 12. AAs of various methods under different numbers of labeled examples per class (*i.e.*, 1, 2, 3, and 4 labeled examples per class). (a) *Indian Pines* dataset. (b) *University of Pavia* dataset. (c) *Salinas* dataset. (d) *Houston University* dataset. (e) *WHU-Hi-HanChuan* dataset. (f) *WHU-Hi-HongHu* dataset.

G. Analysis of Localized and Hierarchical Graph Convolution

In this subsection, we analyze the contributions of the localized graph convolution and hierarchical graph convolution to the proposed ConGCN, respectively. Specifically, we carry out the ablation study on six datasets (*i.e.*, *Indian Pines*, *University of Pavia*, *Salinas*, *Houston University*, *WHU-Hi-HanChuan*, and *WHU-Hi-HongHu* datasets). The number of labeled pixels per class is kept identical to the experimental settings in Section VII-A of the main paper. Concretely, Table XIII exhibits the OAs, AAs, and kappa coefficients obtained by GCN and HGNCN, respectively. It is apparent that the OAs and kappa coefficients of GCN and HGNCN are both lower than those of ConGCN on each dataset. It reveals that both the localized and hierarchical graph convolution operations make an essential contribution to boosting the classification performance. In other words, the representation power of ConGCN is enhanced by jointly employing the localized and hierarchical graph convolution.

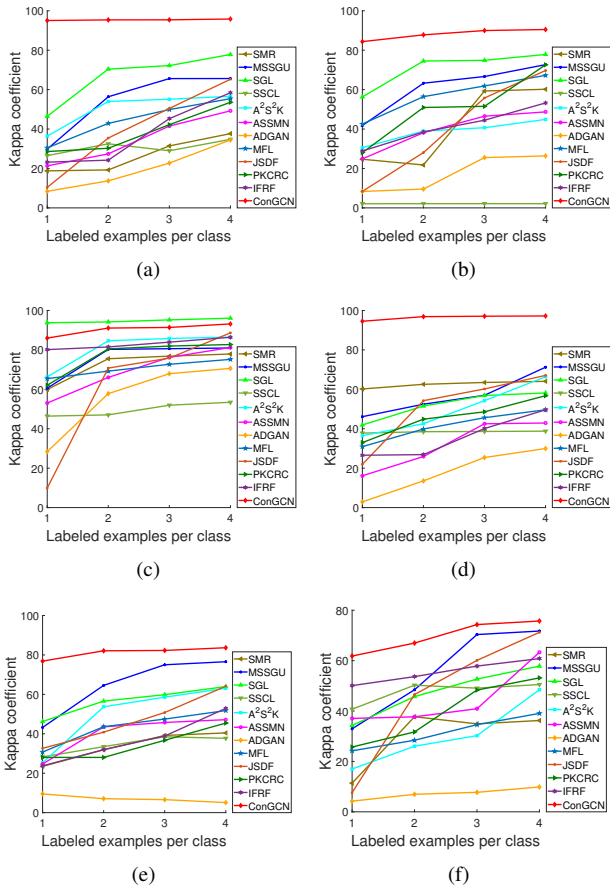


Fig. 13. Kappa coefficients of various methods under different numbers of labeled examples per class (*i.e.*, 1, 2, 3, and 4 labeled examples per class).
 (a) *Indian Pines* dataset. (b) *University of Pavia* dataset. (c) *Salinas* dataset.
 (d) *Houston University* dataset. (e) *WHU-Hi-HanChuan* dataset. (f) *WHU-Hi-HongHu* dataset.

REFERENCES

- [1] Y. Zhong, X. Wang, Y. Xu, S. Wang, T. Jia, X. Hu, J. Zhao, L. Wei, and L. Zhang, "Mini-UAV-borne hyperspectral remote sensing: From observation and processing to applications," *IEEE Geosci. Remote Sens. Mag.*, vol. 6, no. 4, pp. 46–62, Dec. 2018.
- [2] Y. Zhong, X. Hu, C. Luo, X. Wang, J. Zhao, and L. Zhang, "WHU-Hi: UAV-borne hyperspectral with high spatial resolution (H2) benchmark datasets and classifier for precise crop identification based on deep convolutional neural network with CRF," *Remote Sens. Environ.*, vol. 250, p. 112012, Aug. 2020.
- [3] C. Qin, Y. Wu, J. T. Springenberg, A. Brock, J. Donahue, T. Lillicrap, and P. Kohli, "Training generative adversarial networks by solving ordinary differential equations," in *Proc. Conf. Adv. Neural Inf. Process. Syst. (NeurIPS)*, 2020, pp. 5599–5609.
- [4] C. Wang, L. Zhang, W. Wei, and Y. Zhang, "Toward effective hyperspectral image classification using dual-level deep spatial manifold representation," *IEEE Trans. Geosci. Remote Sens.*, early access, Apr. 29, 2021, doi:10.1109/TGRS.2021.3073932.
- [5] Q. Liu, L. Xiao, J. Yang, and Z. Wei, "Multilevel superpixel structured graph U-nets for hyperspectral image classification," *IEEE Trans. Geosci. Remote Sens.*, early access, Sep. 24, 2021, doi:10.1109/TGRS.2021.3112586.
- [6] P. Sellars, A. I. Aviles-Rivero, and C.-B. Schönlieb, "Superpixel contracted graph-based learning for hyperspectral image classification," *IEEE Trans. Geosci. Remote Sens.*, vol. 58, no. 6, pp. 4180–4193, Jun. 2020.
- [7] S. Hou, H. Shi, X. Cao, X. Zhang, and L. Jiao, "Hyperspectral imagery classification based on contrastive learning," *IEEE Trans. Geosci. Remote Sens.*, early access, Dec. 28, 2021, doi:10.1109/TGRS.2021.3139099.
- [8] S. K. Roy, S. Manna, T. Song, and L. Bruzzone, "Attention-based adaptive spectral-spatial kernel ResNet for hyperspectral image classification," *IEEE Trans. Geosci. Remote Sens.*, vol. 59, no. 9, pp. 7831–7843, Sep. 2021.
- [9] D. Wang, B. Du, L. Zhang, and Y. Xu, "Adaptive spectral-spatial multiscale contextual feature extraction for hyperspectral image classification," *IEEE Trans. Geosci. Remote Sens.*, vol. 59, no. 3, pp. 2461–2477, Mar. 2021.
- [10] J. Wang, F. Gao, J. Dong, and Q. Du, "Adaptive dropblock-enhanced generative adversarial networks for hyperspectral image classification," *IEEE Trans. Geosci. Remote Sens.*, vol. 59, no. 6, pp. 5040–5053, Jun. 2021.
- [11] J. Li, X. Huang, P. Gamba, J. M. Bioucas-Dias, L. Zhang, J. A. Benediktsson, and A. Plaza, "Multiple feature learning for hyperspectral image classification," *IEEE Trans. Geosci. Remote Sens.*, vol. 53, no. 3, pp. 1592–1606, Mar. 2015.
- [12] C. Bo, H. Lu, and D. Wang, "Hyperspectral image classification via JCR and SVM models with decision fusion," *IEEE Geosci. Remote Sens. Lett.*, vol. 13, no. 2, pp. 177–181, Feb. 2016.
- [13] J. Liu, Z. Wu, J. Li, A. Plaza, and Y. Yuan, "Probabilistic-kernel collaborative representation for spatial-spectral hyperspectral image classification," *IEEE Trans. Geosci. Remote Sens.*, vol. 54, no. 4, pp. 2371–2384, Apr. 2016.
- [14] X. Kang, S. Li, and J. A. Benediktsson, "Feature extraction of hyperspectral images with image fusion and recursive filtering," *IEEE Trans. Geosci. Remote Sens.*, vol. 52, no. 6, pp. 3742–3752, Jun. 2014.

TABLE XIII

OAs, AAs (%), and Kappa coefficients achieved by different graph convolution networks on six datasets. The best records in each row are **BOLDED**.

Dataset	metrics	GCN	HGCN	ConGCN
<i>Indian Pines</i>	OA	95.67±0.67	95.13±0.72	96.74±0.50
	AA	96.99±0.43	96.89±0.37	97.28±0.29
	kappa	95.05±0.76	94.43±0.81	96.27±0.57
<i>University of Pavia</i>	OA	94.41±1.95	94.28±1.37	95.97±0.90
	AA	95.26±0.63	95.17±0.41	95.14±0.57
	kappa	92.71±2.47	92.54±1.73	94.69±1.17
<i>Salinas</i>	OA	97.33±5.23	97.18±5.55	99.25±0.29
	AA	96.92±6.92	98.66±1.67	99.22±0.19
	kappa	97.01±5.85	96.89±6.09	99.17±0.33
<i>Houston University</i>	OA	96.21±4.30	96.14±4.81	98.61±0.37
	AA	96.49±3.82	96.51±3.98	98.57±0.41
	kappa	95.90±4.66	95.82±5.20	98.49±0.40
<i>WHU-Hi-HanChuan</i>	OA	95.40±0.94	95.21±1.22	97.71±0.58
	AA	94.64±0.98	94.41±1.14	96.92±0.58
	kappa	94.63±1.09	94.40±1.42	97.32±0.68
<i>WHU-Hi-HongHu</i>	OA	95.57±0.87	95.21±1.11	97.32±0.63
	AA	96.37±0.75	96.46±0.92	97.04±0.39
	kappa	94.47±0.84	94.03±1.03	96.63±0.78